

On the effects of radiation on mass transfer in binary stars

Jakub Cehula^{1,2,3*} and Ondřej Pejcha¹

¹Institute of Theoretical Physics, Faculty of Mathematics and Physics, Charles University, V Holešovičkách 2, Prague, 180 00, Czech Republic

²Tartu Observatory, University of Tartu, Tõrvavere, 61602 Tartumaa, Estonia

³Astronomical Institute, Slovak Academy of Sciences, 059 60 Tatranská Lomnica, Slovakia

Accepted 2025 December 18. Received 2025 November 19; in original form 2025 May 13

arXiv:2505.10616v2 [astro-ph.SR] 7 Jan 2026

ABSTRACT

Mass transfer (MT) in binary systems is a common evolutionary process that can significantly affect the structure, evolution, and final fate of both stars. In modeling MT hydrodynamics, it is usually assumed that the critical point of the flow, where the velocity exceeds the local sound speed, coincides with the inner Lagrange point (L1). However, in massive donors where radiative pressure dominates over gas pressure and the Eddington factor Γ_{Edd} can approach or exceed unity, radiation–gas coupling can shift the critical point away from L1, altering the MT rate (\dot{M}_d). We investigate the effects of radiation on MT using time-steady radiative hydrodynamic equations and the von Zeipel theorem. We derive analytical expressions that closely approximate \dot{M}_d , algebraic solutions for simplified cases, and numerical results using a realistic equation of state. Two main differences emerge relative to traditional prescriptions for \dot{M}_d . First, for Roche-lobe-underfilling donors with $\Gamma_{\text{Edd}} \lesssim 1$, radiative momentum exchange leads to an exponential increase of \dot{M}_d as a function of $1 - \Gamma_{\text{Edd}}$. We provide a simple modification of existing prescriptions that captures this effect. Second, the photon tiring limit for super-Eddington outflows is much less restrictive near L1 than in spherical stars. We suggest that donors with super-Eddington, convectively inefficient subsurface layers can drive MT with $-\dot{M}_d \gtrsim 10^{-2} M_\odot \text{ yr}^{-1}$ even before Roche-lobe overflow. We characterize the conditions for this new mode of super-Eddington-boosted MT and discuss its implications for binary evolution, including potential links to nonterminal outbursts of Luminous Blue Variables.

Key words: binaries: close – stars: evolution – stars: mass-loss – radiation: dynamics

1 INTRODUCTION

Massive stars drive cosmic evolution through their winds, photons, and explosions. Their evolutionary journey ultimately leads to the synthesis of new chemical elements and the formation of neutron stars and black holes. Most massive stars exist in gravitationally bound binaries or higher-order multiples (e.g. [Moe & Di Stefano 2017](#)) and mutual interaction between stars can significantly alter their evolution, ultimate fate, and imprint on surroundings (e.g. [Sana et al. 2012](#); [Tauris & van den Heuvel 2023](#); [Marchant & Bodensteiner 2024](#)). Binary stars often interact through mass transfer (MT), where material flows from one star through the first Lagrange point (L1) to its companion. Ongoing MT can be detected by observing the energy released as the material falls toward the companion or by identifying signatures of diffuse gas surrounding the binary system when some material escapes the binary completely. Over time, MT can significantly alter both the internal structures and external appearances of stars, making evolutionary paths impossible for isolated stars. In some cases, MT becomes unstable, triggering common envelope evolution, which is a critical phase in many evolutionary pathways that lead to compact object binaries and gravitational wave progenitors ([Paczynski 1976](#); [Belczynski et al. 2002](#); [Mandel & Broekgaarden 2022](#); [Röpke & De Marco 2023](#)).

One key difference between massive stars and low-mass stars is the significant role of radiation pressure. The increasing importance

of radiation pressure with stellar mass, both inside and outside the photosphere, manifests in relations between global properties of stars, such as the mass–luminosity relation on the main sequence, the intensification of line-driven winds, and positively contributes to the viability of phenomena such as chemically homogeneous evolution (e.g., [Maeder & Meynet 1987](#); [Maeder 1987](#); [Heger & Langer 2000](#); [Vink et al. 2000](#); [Yoon et al. 2006](#)).

Massive stars can exceed the continuum Eddington limit, where the outward frequency-integrated radiative acceleration exceeds the inward gravitational pull. The existence and position of super-Eddington regions depend on density, temperature, and opacity profiles inside the star. Historically, approaching or exceeding the Eddington limit has been argued to be associated with increased mass loss. There is observational evidence that the proximity to the Eddington limit is the physical reason for the onset of Wolf-Rayet-type mass loss (e.g. [Gräfener et al. 2011](#)) and a potential mechanism responsible for luminous blue variable (LBV) eruptions (e.g., [Lamers & Fitzpatrick 1988](#); [Smith & Owocki 2006](#); [Smith et al. 2011](#)).

The simple fact of existence of a super-Eddington region is not sufficient to generate outflows because the energy flux can instead be carried out by convection ([Joss et al. 1973](#)). Near the stellar surface, convection can become inefficient once the required convective velocities approach or exceed the local sound speed. One-dimensional stellar models are able to support limited convectively inefficient super-Eddington regions by means of envelope inflation, density and pressure inversions, and possibly pulsations (e.g., [Glatzel & Kiriakidis 1993](#); [Sanyal et al. 2015](#)). [Owocki et al. \(2004\)](#) argued that the

* E-mail: jakub.cephula@ut.ee

mass-loss rate of any super-Eddington wind driven from the region of inefficient convection would far exceed the photon tiring limit, where all available stellar luminosity is used to lift material from the star to infinity, and such outflow would stagnate at some finite radius and fall back to the star. Consequently, multidimensional effects such as hydrodynamic instabilities and effectively porous envelopes for radiation transfer are likely to significantly alter these spherically symmetric predictions (e.g., Mihalas 1969; Shaviv 2001b; Begelman 2001; Owocki et al. 2004). This was confirmed by time-dependent simulations of Jiang et al. (2015, 2018), which showed complex outflow and inflow patterns with occasional eruptions. Nevertheless, continuum super-Eddington winds can still occur if some additional energy is deposited below the surface, and the photon-tiring limit remains important in these situations (Shaviv 2001a; Owocki et al. 2004, 2017; Quataert et al. 2016; Shen et al. 2016).

The ideas and results on super-Eddington regions in stars rely on the crucial fact that radiative and gravitational accelerations in a spherically symmetric object have the same inverse-square scaling with radius. This is not the case for Roche-lobe-filling stars in binaries, where effective gravity vanishes at the L1 point. Consequently, in a fraction of the stellar envelope, radiative forces can potentially overwhelm gravity and drive much higher MT rates because the photon tiring now needs to overcome much smaller gravitational potential difference. Such a super-Eddington MT boost could play an important role in binary evolution involving massive stars and for explaining the origin of eruptions in LBVs, which are or could have once been a component of a binary system (e.g., Smith & Owocki 2006; Smith & Tombleson 2015; Mahy et al. 2022).

In this paper, our objective is to characterize the effects of radiation pressure on MT through the L1 point. In particular, we are interested in understanding MT from donors with a super-Eddington layer located immediately inside the L1 point, as illustrated in Fig. 1. Our approach builds on our previous work in Cehula & Pejcha (2023, hereafter CP23), where we averaged the three-dimensional equations of hydrodynamics in the plane normal to the axis connecting both stars and solved the resulting one-dimensional two-point boundary value problem. In other words, we solved the structure of the star just interior the L1 point allowing for velocity terms and connecting to the hydrostatic spherically symmetric stellar model at the inner boundary. Here, we modify the method to include radiation. By finding a steady hydrodynamic solution in a gravitational potential near L1, we are in principle able to isolate effects that are inaccessible in the traditional approach, where the MT rate is calculated by post-processing a spherically symmetric stellar model (e.g. Ritter 1988; Kolb & Ritter 1990; Jackson et al. 2017; Marchant et al. 2021).

In Section 2, we introduce the general 3D and 1D time-steady radiation hydrodynamic equations in flux-limited diffusion together with the von Zeipel theorem. In Section 3, we simplify the equations for the limiting cases of hydrostatic equilibrium, small velocities, and adiabaticity. In Section 4, we investigate sub-Eddington donors by constructing analytical estimates and presenting algebraic and numerical solutions. We also illustrate our results on realistic massive donors. In Section 5, we develop the theory of super-Eddington MT boost and apply the concept to a previously calculated binary evolution trajectory. In Section 6, we summarize our findings and discuss the implications and directions of future research.

2 THEORY

Here, we introduce the radiation hydrodynamic equations that govern MT. In Section 2.1, we use general 3D time-steady equations in

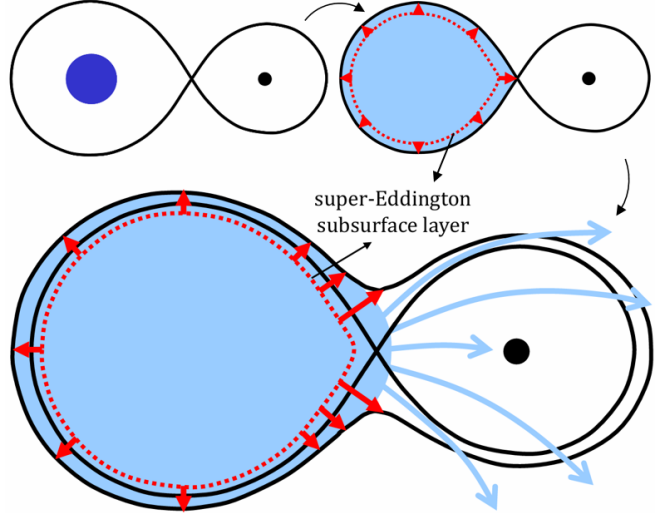


Figure 1. Cartoon illustrating the idea of the super-Eddington mass-transfer boost.

the flux-limited diffusion approximation to derive a general velocity (momentum) equation. In Section 2.2, we reduce the equations to 1D assuming that the flow proceeds through a nozzle around the L1 point. We also compare this case with a spherically symmetric stellar wind. Finally, we introduce the von Zeipel theorem in Section 2.3. This is our crucial assumption, which allows us to reduce the equations to the limiting cases in Section 3, and which we further solve in Section 4.

2.1 General three-dimensional equations

We start with stationary frequency-integrated 3D radiation hydrodynamic equations assuming that radiation has a blackbody spectrum at the local radiation temperature, scattering is negligible, flux mean opacity is equal to Rosseland mean opacity (which is valid in optically thick regions), and using flux-limited diffusion approximation (e.g. Alme & Wilson 1973; Mihalas & Mihalas 1984; Krumholz et al. 2007). The mixed-frame formulation correct to $O(v/c)$ in the streaming, static diffusion, and dynamic diffusion regimes including the Roche potential ϕ_R reads (e.g. Zhang et al. 2011; Calderón et al. 2021)

$$\nabla \cdot (\rho v) = 0, \quad (1a)$$

$$\nabla \cdot (\rho v \otimes v) + \nabla P_{\text{gas}} + \lambda \nabla E_{\text{rad}} = -\rho \nabla \phi_R, \quad (1b)$$

$$\nabla \cdot (\rho \epsilon^* v + P_{\text{gas}} v) + \lambda v \cdot \nabla E_{\text{rad}} = -c \rho \kappa_P (a_{\text{rad}} T^4 - E_{\text{rad}}^{(0)}), \quad (1c)$$

$$\begin{aligned} \nabla \cdot \left(\frac{3-f}{2} E_{\text{rad}} v \right) - \lambda v \cdot \nabla E_{\text{rad}} &= c \rho \kappa_P (a_{\text{rad}} T^4 - E_{\text{rad}}^{(0)}) \\ &+ \nabla \cdot \left(\frac{c \lambda}{\rho \kappa_R} \nabla E_{\text{rad}} \right), \end{aligned} \quad (1d)$$

$$F_{\text{rad}}^{(0)} = -\frac{c \lambda}{\rho \kappa_R} \nabla E_{\text{rad}}^{(0)}, \quad (1e)$$

$$P_{\text{rad}}^{(0)} = f E_{\text{rad}}^{(0)}, \quad (1f)$$

where the quantities with the superscript (0) are evaluated in the co-moving frame while quantities without it in the lab frame. Gas density, thermal pressure, and velocity are denoted by ρ , P_{gas} , and v , respectively. Radiation energy density, pressure, and flux are denoted

by E_{rad} , P_{rad} , and \mathbf{F}_{rad} , respectively. Next, c is the speed of light, a_{rad} the radiation constant, T the gas temperature, and κ_P and κ_R , the Planck mean and Rosseland mean opacities, respectively. It is worth noting that the Planck mean and Rosseland mean interaction coefficients $\rho\kappa_P$ and $\rho\kappa_R$ (in units of cm^{-1}) are always evaluated in the co-moving frame. The total gas specific energy ϵ^* comprises of three components, internal, kinetic, and potential,

$$\epsilon^* = \epsilon_{\text{gas}} + \frac{1}{2} |\mathbf{v}|^2 + \phi_R, \quad (2)$$

where ϵ_{gas} is the gas (internal) specific energy in units of erg g^{-1} . The flux limiter λ and the Eddington factor f are defined by (Levermore & Pomraning 1981)

$$\lambda = \frac{2+R}{6+3R+R^2}, \quad f = \lambda + \lambda^2 R^2, \quad R = \frac{|\nabla E_{\text{rad}}^{(0)}|}{\rho\kappa_R E_{\text{rad}}^{(0)}}. \quad (3)$$

Radiation energy density in the lab frame and the co-moving frame are related by (Zhang et al. 2011)

$$E_{\text{rad}}^{(0)} = E_{\text{rad}} - \frac{2}{c^2} \mathbf{v} \cdot \mathbf{F}_{\text{rad}}^{(0)} + O\left(\frac{v^2}{c^2}\right) = E_{\text{rad}} + 2 \frac{\lambda}{\rho\kappa_R} \frac{\mathbf{v}}{c} \cdot \nabla E_{\text{rad}} + O\left(\frac{v^2}{c^2}\right). \quad (4)$$

In some parts of our work we further assume ideal gas equation of state (EOS),

$$P_{\text{gas}} = \frac{k}{\bar{m}} T \rho = c_{T,\text{gas}}^2 \rho, \quad \epsilon_{\text{gas}} = \frac{1}{\gamma-1} \frac{k}{\bar{m}} T = \frac{1}{\gamma-1} c_{T,\text{gas}}^2, \quad (5)$$

where k is the Boltzmann constant, \bar{m} is the mean mass of a gas particle, $c_{T,\text{gas}}$ is the gas isothermal sound speed, and $\gamma = c_P/c_V$, where c_P and c_V are dimensionless heat capacities at constant pressure and volume.

Based on these assumptions, we can derive a velocity equation for ideal gas in the form following Lubow & Shu (1975, eq. 10), which elucidates the terms contributing to the existence and position of the critical point,

$$\nabla \cdot \mathbf{v} = \frac{|\mathbf{v}|^3 \nabla \cdot (\mathbf{v}/|\mathbf{v}|) - (\gamma-1) |\mathbf{v}| q_{\text{rad}} + \mathbf{v} \cdot \mathbf{f}_{\text{rad}} - \mathbf{v} \cdot \nabla \phi_R}{|\mathbf{v}|^2 - c_{s,\text{gas}}^2}, \quad (6)$$

where we denote

$$q_{\text{rad}} \equiv -\frac{c}{|\mathbf{v}|} \kappa_P \left(a_{\text{rad}} T^4 - E_{\text{rad}}^{(0)} \right), \quad (7)$$

$$\mathbf{f}_{\text{rad}} \equiv -\frac{\lambda}{\rho} \nabla E_{\text{rad}} = \frac{\kappa_R}{c} (\mathbf{F}_{\text{rad}} - \mathbf{F}_{\text{adv}}), \quad (8)$$

and where we subtract the advective flux $\mathbf{F}_{\text{adv}} \equiv \mathbf{v} E_{\text{rad}} + \mathbf{v} \cdot \mathbf{P}_{\text{rad}}$ from the lab frame radiative flux \mathbf{F}_{rad} , where \mathbf{P}_{rad} is the radiation pressure tensor (Krumholz et al. 2007). The gas adiabatic sound speed $c_{s,\text{gas}}$ reads

$$c_{s,\text{gas}}^2 = \gamma \frac{P_{\text{gas}}}{\rho}. \quad (9)$$

The velocity equation for a general EOS (A8) together with its derivation can be found in Appendix A. This more complete equation differs only by additional terms arising from the thermodynamic derivatives of the EOS, which do not fundamentally change the structure.

There are three differences between our velocity equation (6) and the isothermal velocity equation of Lubow & Shu (1975, their eq. 10). First, our velocity equation includes the term $\mathbf{v} \cdot \mathbf{f}_{\text{rad}}$ that accounts for the increase in radiation momentum originating from the radiation pressure. Second, our equation involves the term $-(\gamma-1) |\mathbf{v}| q_{\text{rad}}$

that accounts for the gas specific heating/cooling rate (in units of $\text{erg g}^{-1} \text{s}^{-1}$) due to energy exchange between the gas and radiation. Third, our critical velocity is the gas adiabatic sound speed $c_{s,\text{gas}}$ instead of the gas isothermal sound speed $c_{T,\text{gas}}$.

The sonic surface ($|\mathbf{v}| = c_{s,\text{gas}}$) is located at a region where the right-hand-side numerator of equation (6) vanishes,

$$|\mathbf{v}|^2 \nabla \cdot \left(\frac{\mathbf{v}}{|\mathbf{v}|} \right) = (\gamma-1) q_{\text{rad}} + \frac{\mathbf{v}}{|\mathbf{v}|} \cdot (\nabla \phi_R - \mathbf{f}_{\text{rad}}). \quad (10)$$

Thus, heating/cooling due to energy exchange between gas and radiation q_{rad} and radiation momentum boost \mathbf{f}_{rad} can move the location of the sonic surface away from the L1 point ($\nabla \phi_R = 0$).

2.2 General one-dimensional equations

Let us now assume that the gas flows through a nozzle oriented along the x axis and with a cross-section denoted by $Q(x)$. In CP23, we calculated $Q(x)$ based on the Roche potential and thermodynamic properties of the gas flowing to the L1 point. Assuming that all quantities are constant at a given $Q(x)$, we can reduce the set of 3D equations (1) to the set of 1D equations (see Appendix B for details),

$$\frac{1}{v} \frac{dv}{dx} + \frac{1}{\rho} \frac{d\rho}{dx} + \frac{1}{Q} \frac{dQ}{dx} = 0, \quad (11a)$$

$$v \frac{dv}{dx} + \frac{1}{\rho} \frac{dP_{\text{gas}}}{dx} = f_{\text{rad}} - \frac{d\phi_R}{dx}, \quad (11b)$$

$$\frac{d\epsilon_{\text{gas}}}{dx} - \frac{P_{\text{gas}}}{\rho} \frac{1}{\rho} \frac{d\rho}{dx} = q_{\text{rad}}, \quad (11c)$$

$$L_N = \left[\frac{c}{\kappa_R} f_{\text{rad}} + \left(\rho \epsilon^* + P_{\text{gas}} + \frac{3-f}{2} E_{\text{rad}} \right) v \right] Q, \quad (11d)$$

where $L_N = \text{const.}$ is the total energy flux being transferred through the nozzle and comprises of the radiative $L_{N,\text{rad}} = (c/\kappa_R) f_{\text{rad}} Q$ and advective $L_{N,\text{adv}} = (\rho \epsilon^* + P_{\text{gas}} + (3-f) E_{\text{rad}}/2) v Q$ part. Instead of equation (1e) we can use the 1D version of equation (8), i.e.

$$f_{\text{rad}} = -\frac{\lambda}{\rho} \frac{dE_{\text{rad}}}{dx}, \quad (12)$$

and equation (1f) remains unchanged. The donor's mass loss rate is given by (see also CP23)

$$-\dot{M}_d = v \rho Q. \quad (13)$$

Assuming ideal gas EOS (equation 5) we can derive the velocity equation in the following form

$$\frac{1}{v} \frac{dv}{dx} = \frac{\frac{c_{s,\text{gas}}^2}{Q} \frac{1}{Q} \frac{dQ}{dx} - (\gamma-1) q_{\text{rad}} + f_{\text{rad}} - \frac{d\phi_R}{dx}}{v^2 - c_{s,\text{gas}}^2}. \quad (14)$$

The velocity equation for a general EOS can be found in Appendix B.

In a special case of spherically symmetric and isolated donor (star), i.e. spherically symmetric mass loss (nozzle), we can write $x \rightarrow r$, $Q \rightarrow 4\pi r^2$, and $\phi_R \rightarrow \phi_d = -GM_d/r$, where r is the radial coordinate, ϕ_d is the donor's gravitational potential, G is the gravitational constant, and M_d is donor's mass. This leads to the velocity equation in the form

$$\frac{1}{v} \frac{dv}{dr} = \frac{\frac{c_{s,\text{gas}}^2}{r} \frac{2}{r} - (\gamma-1) q_{\text{rad}} + f_{\text{rad}} - \frac{GM_d}{r^2}}{v^2 - c_{s,\text{gas}}^2}, \quad (15)$$

which is the general form of the momentum equation of a spherically symmetric stellar wind with energy input (q_{rad}) and momentum

input (f_{rad}) (Lamers & Cassinelli 1999, eq. 4.18). Moreover, considering equation (11d), we get $f_{\text{rad}} = (L_{\text{d,rad}}/L_{\text{d,Edd}})(GM_{\text{d}}/r^2) = (L_{\text{d,rad}}/L_{\text{d,Edd}})(d\phi_{\text{R}}/dr)$, where $L_{\text{d,rad}}$ is the donor's radiative (diffusive) luminosity and $L_{\text{d,Edd}}$ is the donor's Eddington luminosity and we have used $L_{\text{N}} = L_{\text{d}}$, where L_{d} is the donor's total luminosity and $L_{\text{d,Edd}} = 4\pi c GM_{\text{d}}/\kappa_{\text{R}}$.

2.3 The von Zeipel theorem

The set of 1D radiation hydrodynamic equations (11) can be further simplified. We can use an extension of the von Zeipel theorem, which states that the radiative flux in a uniformly rotating star is proportional to the local effective gravity (von Zeipel 1924), and write for the donor's envelope (see also recent works by Fabry et al. 2022, 2023)

$$\mathbf{F}_{\text{rad}} = \frac{L_{\text{rad}}(\phi_{\text{R}})}{4\pi GM(\phi_{\text{R}})} \nabla \phi_{\text{R}}, \quad (16)$$

where $L_{\text{rad}}(\phi_{\text{R}})$ and $M(\phi_{\text{R}})$ are the donor's radiative luminosity and mass coordinates, respectively, corresponding to a given equipotential ϕ_{R} .

Within this approximation and neglecting the advective term in equation (8), we can write

$$\mathbf{f}_{\text{rad}} = \frac{L_{\text{rad}}(\phi_{\text{R}})}{L_{\text{Edd}}(\phi_{\text{R}})} \nabla \phi_{\text{R}} \equiv \Gamma_{\text{Edd}}(\phi_{\text{R}}) \nabla \phi_{\text{R}}, \quad (17)$$

where $L_{\text{Edd}}(\phi_{\text{R}})$ is the donor's Eddington luminosity corresponding to a given ϕ_{R} and we define the corresponding Eddington ratio $\Gamma_{\text{Edd}}(\phi_{\text{R}})$, i.e. the ratio of the radiative over Eddington luminosity at a given ϕ_{R} .

The fundamental assumption underlying von Zeipel approximation is that the donor is barotropic, i.e. ρ, T , etc. are only functions of ϕ_{R} (von Zeipel 1924) and that the effects of convection are ignored. The application of this theorem to Roche-lobe-filling stars also seems problematic, because the von Zeipel theorem predicts zero radiative flux at the L1 point. We will further discuss the limitations in Section 6.

3 LIMITING CASES

In this section, we further simplify the 1D radiation hydrodynamic equations governing the MT through the nozzle around L1 that were introduced in Section 2.2. The key assumption we use in all limiting cases is the von Zeipel theorem (Section 2.3). We first show the hydrostatic case in Section 3.1, which subsequently motivates the small-velocity (small- v) case ($v \ll c$) in Section 3.2. We then move to the adiabatic case where there is no energy exchange between gas and radiation in Section 3.3.

3.1 Optically-thick hydrostatic case

In the limit of $v \rightarrow 0$ the co-moving frame becomes identical with the lab frame and the continuity equation (11a) now becomes trivial, $v = 0$. Also, q_{rad} (equation 7) in equation (11c) has to be finite, thus $E_{\text{rad}} \rightarrow a_{\text{rad}}T^4$. Assuming optically thick limit, i.e. $R \rightarrow 0, \lambda \rightarrow 1/3$, and $f \rightarrow 1/3$ (equation 3), we further obtain $P_{\text{rad}} \rightarrow E_{\text{rad}}/3$ in equation (1f). Finally, using the von Zeipel theorem either in the form of equation (16) or (17) and considering equations (11b, 12) leads to the system of six equations for six unknowns (three related

to gas, ρ, P_{gas}, v , and three to radiation $P_{\text{rad}}, E_{\text{rad}}, f_{\text{rad}}$), where only two equations are non-trivial due to our approximations

$$\frac{1}{\rho} \frac{dP_{\text{gas}}}{dx} = -(1 - \Gamma_{\text{Edd}}) \frac{d\phi_{\text{R}}}{dx}, \quad (18a)$$

$$\frac{1}{\rho} \frac{dP_{\text{rad}}}{dx} = -\Gamma_{\text{Edd}} \frac{d\phi_{\text{R}}}{dx}, \quad (18b)$$

with

$$v = 0, P_{\text{rad}} = \frac{1}{3} a_{\text{rad}} T^4, E_{\text{rad}} = a_{\text{rad}} T^4, f_{\text{rad}} = \Gamma_{\text{Edd}} \frac{d\phi_{\text{R}}}{dx}. \quad (19)$$

Instead of equation (18b), we can equivalently use $F_{\text{rad}} = L/(4\pi GM)(d\phi_{\text{R}}/dx)$.

Using the above set of equations, we can in principle reconstruct part of the donor's hydrostatic envelope close to the L1 point, specifically, between some point x_0 and the L1 point located at $x_1, x_0 < x_1$. In order to close the system of equations we still need an EOS for P_{gas} and two boundary conditions: $\rho(x_0) = \rho_0$ and $T(x_0) = T_0$ that need to be taken from the underlying hydrostatic structure of a stellar evolution code. We also need to evaluate the Eddington ratio Γ_{Edd} (equation 17). The exact way to connect the x coordinate with the potential ϕ and consecutively with the radius r was explained in CP23 and will also be discussed later in Section 4.1.

3.2 Optically-thick, $v \ll c$ case

We can generalize the previous case to a situation where there is a slow but nonzero velocity, $v \ll c$. We apply assumptions similar to those in the hydrostatic case, but in order to obtain the continuity equation, we need a prescription for the cross section of the nozzle Q . In our previous work (CP23, but see also Meyer & Meyer-Hofmeister 1983), we assumed $Q \propto c_{T,\text{gas}}^2 \propto P_{\text{gas}}/\rho$, which assumes that the gas is in adiabatic hydrostatic equilibrium in the plane perpendicular to to flow toward L1. For simplicity, we apply the same assumption here and we arrive at the following set of equations

$$\frac{1}{v} \frac{dv}{dx} + \frac{1}{P_{\text{gas}}} \frac{dP_{\text{gas}}}{dx} = 0, \quad (20a)$$

$$v \frac{dv}{dx} + \frac{1}{\rho} \frac{dP_{\text{gas}}}{dx} = -(1 - \Gamma_{\text{Edd}}) \frac{d\phi_{\text{R}}}{dx}, \quad (20b)$$

$$\frac{1}{\rho} \frac{dP_{\text{rad}}}{dx} = -\Gamma_{\text{Edd}} \frac{d\phi_{\text{R}}}{dx}, \quad (20c)$$

with

$$E_{\text{rad}} = a_{\text{rad}} T^4, P_{\text{rad}} = \frac{E_{\text{rad}}}{3}, f_{\text{rad}} = \frac{\kappa_{\text{R}}}{c} F_{\text{rad}} = \Gamma_{\text{Edd}} \frac{d\phi_{\text{R}}}{dx}, \quad (21)$$

where we have three non-trivial (differential) equations for three unknowns related to gas properties and the radiation unknowns are trivially (algebraically) related. This is a two-point boundary value problem. We have two boundary conditions at $x_0, \rho(x_0) = \rho_0$ and $T(x_0) = T_0$, which are fixed to values from a 1D hydrostatic model. The third boundary condition is applied at $x_{\text{crit}}, v^2(x_{\text{crit}}) = P_{\text{gas}}(x_{\text{crit}})/\rho(x_{\text{crit}})$, which is the critical point either where $\Gamma_{\text{Edd}} = 1$ or at the point L1, where $d\phi_{\text{R}}/dx = 0$. The resulting MT rate is calculated using equation (13), where the exact value of Q is calculated using an analytical estimate (equation 30) derived later in Section 4.2.

3.3 Optically-thick, adiabatic, $v \ll c$ case

Let us now consider the same case as before, but instead of equation (20c) we now assume that there is no energy exchange between radiation and gas, i.e. $q_{\text{rad}} = 0$ in equation (11c), and the gas flow is

adiabatic. There can still be momentum exchange between gas and radiation. Thus, only the energy equation changes and we can write

$$\frac{1}{v} \frac{dv}{dx} + \frac{1}{P_{\text{gas}}} \frac{dP_{\text{gas}}}{dx} = 0, \quad (22a)$$

$$v \frac{dv}{dx} + \frac{1}{\rho} \frac{dP_{\text{gas}}}{dx} = -(1 - \Gamma_{\text{Edd}}) \frac{d\phi_R}{dx}, \quad (22b)$$

$$\frac{d\epsilon_{\text{gas}}}{dx} - \frac{P_{\text{gas}}}{\rho} \frac{1}{\rho} \frac{d\rho}{dx} = 0, \quad (22c)$$

with

$$E_{\text{rad}} = a_{\text{rad}} T^4, \quad P_{\text{rad}} = \frac{E_{\text{rad}}}{3}, \quad f_{\text{rad}} = \frac{\kappa_R}{c} F_{\text{rad}} = \Gamma_{\text{Edd}} \frac{d\phi_R}{dx}, \quad (23)$$

and the same boundary conditions as in the previous case (Sec. 3.2, equation 20).

4 SUB-EDDINGTON MASS TRANSFER

Our goal in this Section is to provide solutions to equations outlined in Section 2 and 3 under the assumption that the MT is sub-Eddington. Specifically, this means that when we follow the solution from an interior point, the first critical point we encounter is due to the potential flattening at L1. We discuss situations where $\Gamma_{\text{Edd}} > 1$ inside of L1 in Section 5.

This Section begins by first discussing how to match our solutions to an underlying hydrostatic stellar model (Section 4.1). Then we proceed to formulate analytic estimates of the relevant quantities to develop an intuitive understanding of the expected results (Section 4.2). After that, we present several cases where the equations permit algebraic solutions, which are possible for isothermal and ideal gas assumptions relevant for optically thin and optically thick situations (Section 4.3). Next, we present numerical solutions with a realistic EOS and illustrate the results on two massive stars undergoing MT (Section 4.4). Finally, we summarize our results and compare them with previous work (Section 4.5).

4.1 Relation to hydrostatic structure

An important aspect of our model is the connection between the hydrodynamical mass flow around L1 and the underlying hydrostatic donor envelope structure calculated using a stellar evolution code. Similarly to CP23, we notice that all the limiting cases of our model that we are able to solve, sets of equations (20) and (22), can be reformulated so that the Roche potential ϕ_R becomes the independent variable instead of the coordinate x , allowing us to completely omit the coordinate x . This is what we do in practice in this paper. The mapping between ϕ and r is based on the assumption that equipotentials can be related to spheres with the same equivalent volume. In this work, we use the higher order approximation derived by Jackson et al. (2017) to make the correspondence, see equation (C5). We denote the radius corresponding to the inner boundary of our model at ϕ_0 , or also x_0 , by R_0 . The radius corresponding to the equipotential passing through the L1 point with ϕ_1 is R_L .

If the photosphere is above the L1 point, $R_d > R_L$, we have a Roche-lobe-overfilling donor and a regime that has traditionally been labeled as optically thick. In this case, we calculate the potential difference corresponding to R_0 as

$$\phi_1 - \phi_0 \equiv \int_{R_0}^{R_L} d\bar{\phi} = - \int_{R_0}^{R_L} \frac{d\bar{P}}{\bar{\rho}}, \quad (24)$$

where \bar{P} is the hydrostatic total pressure inside of the donor.

If the photosphere is below the L1 point, $R_d < R_L$, we have a Roche-lobe-underfilling donor and an optically thin regime. In this case, we take the inner boundary of our model to be the donor's photosphere (unlike CP23) and we calculate the potential difference corresponding to $R_0 = R_d$ according to

$$\phi_1 - \phi_0 \equiv \phi_V(R_L) - \phi_V(R_d), \quad (25)$$

where ϕ_V is the equipotential reached by a donor of radius r_V .

In the optically thick regime, it is useful to express the distance between R_0 and R_L (or equivalently between ϕ_0 and ϕ_1 , or x_0 and x_1) by the number of pressure scale heights ΔN_{HP} . We define the pressure scale height number N_{HP} for the donor's interior by

$$N_{HP}(r) \equiv \int_r^{R_d} \frac{dr'}{H_P(r')}, \quad \text{for } r \leq R_d \quad (26)$$

where H_P is the pressure scale height. We see that $N_{HP}(R_d) = 0$ and that N_{HP} increases inward and decreases outward. Hence, for a Roche-lobe-overflowing donor we have

$$\Delta N_{HP} = N_{HP}(R_0) - N_{HP}(R_L) = \int_{R_0}^{R_L} \frac{dr}{H_P}. \quad (27)$$

Finally, let us also explain how we calculate the Eddington factor Γ_{Edd} . The usage of the von Zeipel theorem does not change the value of the Eddington factor. Thus, in the optically thick regime in the donor's interior we calculate it according to (e.g. Sanyal et al. 2015)

$$\Gamma_{\text{Edd}} = \frac{L_{\text{rad}}}{L_{\text{Edd}}} = \frac{4\bar{P}_{\text{rad}}}{\bar{P}} \bar{\nabla}_T, \quad (28)$$

where \bar{P}_{rad} is the hydrostatic radiative pressure and $\bar{\nabla}_T$ is the actual hydrostatic temperature gradient. In the optically thin regime outside the donor we use a simple model, where we assume Γ_{Edd} to be constant and take the value at the photosphere.

4.2 Analytic estimates

The sets of equations (20) or (22) cannot be analytically solved for a general EOS, but we can still analytically estimate the quantity of main interest, $-\dot{M}_d = Q\rho v$ (equation 13). We need to know the underlying hydrostatic structure of the donor from a 1D stellar evolution code, such as the hydrostatic stellar quantities $\bar{\rho}$, \bar{P}_{gas} as a function of stellar radius r or alternatively the stellar gravitational potential $\bar{\phi}$. We also need to know the gas cross-section Q . We need to evaluate \dot{M}_d at one point, and the easiest choice is the critical point located where the right-hand side of equation (20b) vanishes. If the Eddington limit is not reached, then the critical point occurs at the Roche-lobe radius R_L that corresponds to $\bar{\phi}(R_L) = \phi_1$, where ϕ_1 is the Roche potential at L1. Combining equations (20a) and (20b) we see that the critical velocity $v_{\text{crit}} \equiv v(x_{\text{crit}})$ is given by $v_{\text{crit}}^2 = c_{T,\text{gas}}^2 = P_{\text{gas}}/\rho$. Now, we need to express the hydrodynamic values P_{gas} , ρ , which we a priori do not know, as functions of the hydrostatic values \bar{P}_{gas} , $\bar{\rho}$, which we know from a stellar evolution code. Considering the simple case of an isothermal gas (see Sec. 5.1 in CP23, or also Sec. 3.1.3 in Lamers & Cassinelli 1999) we can approximately write $P_{\text{gas}} = \bar{P}_{\text{gas}}/\sqrt{e}$ and $\rho = \bar{\rho}/\sqrt{e}$ at the critical point.

In order to approximate Q we consider the lowest order approximation of the Roche potential in the yz -plane

$$\phi_R(x, y, z) = \phi_R^x(x) + \frac{B}{2}y^2 + \frac{C}{2}z^2, \quad (29)$$

where the centers of the two stars lie on the x axis and the orbital plane

6 Cehula & Pejcha

is the xy plane (CP23). The cross-section Q can then be approximated as

$$Q \equiv \frac{dQ}{d\phi} \Big|_{L1} \frac{P_{\text{gas}}}{\rho}. \quad (30)$$

If we assume Γ_{Edd} to be roughly constant in the yz -plane then the potential is effectively lower by a factor of $(1 - \Gamma_{\text{Edd}})$ and it is equivalent to assume $B \rightarrow (1 - \Gamma_{\text{Edd}})B$ and $C \rightarrow (1 - \Gamma_{\text{Edd}})C$. In such a case we can write (see the derivation of Q_ρ in CP23)

$$\frac{dQ}{d\phi} \Big|_{L1} = \frac{1}{1 - \Gamma_{\text{Edd}}} \frac{2\pi}{\sqrt{BC}} \Big|_{r=R_L}. \quad (31)$$

We see that Q diverges for $\Gamma_{\text{Edd}} \rightarrow 1$.

Nevertheless, if the Eddington limit is not reached and using the definition of Q in equations (30) and (31), \dot{M}_d in equation (13) can be approximated as

$$-\dot{M}_d \approx \dot{M}_{\text{an, thick}} \equiv \frac{1}{1 - \Gamma_{\text{Edd}}} \frac{1}{\sqrt{e}} \frac{2\pi}{\sqrt{BC}} \frac{\bar{P}_{\text{gas}}^{3/2}}{\rho^{1/2}} \Big|_{r=R_L}. \quad (32)$$

This expression can be evaluated only for $r \leq R_d$ and therefore applies only to a Roche-lobe-overflowing donor ($R_L \leq R_d$). Consequently, we follow tradition and refer to this quantity as the optically thick MT rate. We will derive a separate expression for $r \geq R_d$ in Section 4.3.1, equation (36).

4.3 Algebraic solutions

We obtain algebraic solutions for two specific simplifications: isothermal gas (Section 4.3.1), which provides a solution in the optically thin regime, and ideal gas (Section 4.3.2).

4.3.1 Isothermal gas

Let us first consider a simple case where P_{gas} is given by ideal gas law (equation 5) and the temperature T is constant. In this case, the nozzle cross-section Q given by equation (30) is constant and the sets of equations (20) or (22) reduce to

$$\frac{d \ln v}{dx} + \frac{d \ln \rho}{dx} = 0, \quad (33a)$$

$$v^2 \frac{d \ln v}{dx} + c_{T,\text{gas}}^2 \frac{d \ln \rho}{dx} = -(1 - \Gamma_{\text{Edd}}) \frac{d\phi_R}{dx}, \quad (33b)$$

$$T = T_0 = \text{const}, \quad (33c)$$

where instead of the energy equation (20c) or (22c) we assume T is constant. The algebraic solution of this set of equations can be written in the form

$$\frac{1}{2} \left[\left(\frac{v(x)}{c_{T,\text{gas}}} \right)^2 - \left(\frac{v_0}{c_{T,\text{gas}}} \right)^2 \right] - \ln \frac{v(x)}{v_0} = -(1 - \Gamma_{\text{Edd}}) \frac{\phi_R^x(x) - \phi_0}{c_{T,\text{gas}}^2}, \quad (34a)$$

$$\frac{\rho(x)}{\rho_0} = \frac{v_0}{v(x)}, \quad (34b)$$

where we start at $x = x_0$, $\phi_0 = \phi_R^x(x_0)$, $\rho_0 = \rho(x_0)$, $v_0 \equiv v(x_0)$, and we end at $x = x_1$ (the L1 point), provided that $\Gamma_{\text{Edd}} < 1$, where $v(x_1) = c_{T,\text{gas}}$. The velocity v_0 is the solution of the algebraic equation

$$\frac{1}{2} \left(\frac{v_0}{c_{T,\text{gas}}} \right)^2 - \ln \frac{v_0}{c_{T,\text{gas}}} = (1 - \Gamma_{\text{Edd}}) \frac{\phi_1 - \phi_0}{c_{T,\text{gas}}^2} + \frac{1}{2}. \quad (35)$$

The only difference between this isothermal limit and the isothermal limit in CP23 is that the solution here includes the momentum exchange between gas and radiation. Therefore, the potential difference the gas has to cover between x_0 and x_1 (L1) is multiplied by a factor of $(1 - \Gamma_{\text{Edd}})$ and thus somewhat reduced: $(\phi_1 - \phi_0)/c_{T,\text{gas}}^2 \rightarrow (1 - \Gamma_{\text{Edd}})(\phi_1 - \phi_0)/c_{T,\text{gas}}^2$. The isothermal case in CP23 is equivalent to the optically thin MT rate of Ritter (1988), or its improved version of Jackson et al. (2017), depending on how we choose to approximate the difference between the potentials at the L1 point ϕ_1 and the photosphere ϕ_{ph} . Thus, the MT rate corresponding to the isothermal case with radiation is

$$-\dot{M}_d = \dot{M}_{\text{an, thin}} \equiv \dot{M}_0 \exp \left[-(1 - \Gamma_{\text{Edd}}) \frac{\phi_1 - \phi_{\text{ph}}}{c_{T,\text{gas}}^2} \right], \quad (36)$$

where $\dot{M}_0 = \frac{1}{1 - \Gamma_{\text{Edd}}} \frac{1}{\sqrt{e}} \frac{2\pi}{\sqrt{BC}} \frac{P_{\text{gas, ph}}^{3/2}}{\rho_{\text{ph}}^{1/2}}$,

where $P_{\text{gas, ph}}$ and ρ_{ph} are the photosphere gas pressure and density, respectively. We will use this optically thin analytical estimate for Roche-lobe-underfilling donors, $R_d \leq R_L$ and $\phi_{\text{ph}} \leq \phi_1$, for example in Section 4.4.2.

It should be noted that the factor $1 - \Gamma_{\text{Edd}}$ is present not only in the expression for \dot{M}_0 , but also in the exponential factor in equation (36), leading to the exponential dependence of \dot{M}_d on $1 - \Gamma_{\text{Edd}}$. For example, for a photosphere located about four scale heights below L1, $(\phi_1 - \phi_{\text{ph}})/c_{T,\text{gas}}^2 \approx 4$, an Eddington factor of $\Gamma_{\text{Edd}} = 0.5$ will lead to an increase in \dot{M}_d by a factor of $2e^2 \approx 15$. This means that Roche-lobe-underfilling stars with high Γ_{Edd} will exhibit significantly increased \dot{M}_d compared to existing prescriptions.

4.3.2 Ideal gas

Here, we assume an ideal gas EOS (equation 5) for P_{gas} . However, applying this assumption in the small- v case (Section 3.2, equations 20), does not yield an algebraic solution. Instead, we focus on the adiabatic case (Section 3.3, equations 22), which gives

$$\frac{d \ln v}{dx} + \frac{d \ln \rho}{dx} + \frac{d \ln T}{dx} = 0, \quad (37a)$$

$$v^2 \frac{d \ln v}{dx} + \gamma c_{T,\text{gas}}^2 \frac{d \ln \rho}{dx} = -(1 - \Gamma_{\text{Edd}}) \frac{d\phi_R}{dx}, \quad (37b)$$

$$\frac{d \ln \rho}{dx} - \frac{1}{\gamma - 1} \frac{d \ln T}{dx} = 0. \quad (37c)$$

Again as before, the inner boundary is at $x = x_0$ and the outer at $x = x_1$, i.e. the L1 point, provided that $\Gamma_{\text{Edd}} < 1$. The boundary conditions are $\rho(x_0) = \rho_0$, $T(x_0) = T_0$, and $v^2(x_1) = c_{T,\text{gas}}^2(x_1) = kT(x_1)/\bar{m}$. The above set of equations can be solved algebraically,

$$\frac{1}{2} \left[\left(\frac{v}{c_0} \right)^2 - \left(\frac{v_0}{c_0} \right)^2 \right] + \frac{\gamma}{\gamma - 1} \left[\left(\frac{v_0}{v} \right)^{\frac{\gamma-1}{\gamma}} - 1 \right] = -(1 - \Gamma_{\text{Edd}}) \frac{\phi_R^x - \phi_0}{c_0^2}, \quad (38a)$$

$$\rho = \left(\frac{v_0}{v} \right)^{\frac{1}{\gamma}} \rho_0, \quad (38b)$$

$$T = \left(\frac{v_0}{v} \right)^{\frac{\gamma-1}{\gamma}} T_0, \quad (38c)$$

where $c_0^2 \equiv c_{T,\text{gas}}^2(x_0) = kT_0/\bar{m}$ and v_0 is the solution of

$$\frac{3\gamma - 1}{2(\gamma - 1)} \left(\frac{v_0}{c_0} \right)^{\frac{2(\gamma-1)}{3\gamma-1}} - \frac{1}{2} \left(\frac{v_0}{c_0} \right)^2 = -(1 - \Gamma_{\text{Edd}}) \frac{\phi_1 - \phi_0}{c_0^2} + \frac{\gamma}{\gamma - 1}. \quad (39)$$

As before, compared to the ideal gas limit of CP23, the only difference is that the current ideal gas case includes momentum exchange

between gas and radiation. Consequently, the potential difference is reduced: $(\phi_1 - \phi_0)/c_{T,\text{gas}}^2 \rightarrow (1 - \Gamma_{\text{Edd}})(\phi_1 - \phi_0)/c_{T,\text{gas}}^2$. Therefore, we do not discuss this case further in this paper and refer the reader to CP23 for more details.

4.4 Numerical solution for a realistic equation of state

For a general EOS, we solve the set of hydrodynamic equations (20) or (22) using the same framework we developed in CP23 based on a relaxation method of Press et al. (2007, Chapter 18). The realistic EOS is adopted from the MESA eos module (Paxton et al. 2011, 2013, 2015, 2018, 2019). Depending on the metallicity Z and the position in the ρT plane, one of the following components is used: OPAL/SCVH (Rogers & Nayfonov 2002; Saumon et al. 1995), Free EOS (Irwin 2008), HELM (Timmes & Sweaty 2000), PC (Potekhin & Chabrier 2010), Skye (Jermyn et al. 2021), or CMS (Chabrier et al. 2019). Following the tutorial by Timmes (2021), we construct a table with all relevant thermodynamic variables. We interpolate in the table using bilinear interpolation (Press et al. 2007, Chapter 3). We refer the reader to our original work (CP23) for more details.

In what follows, we compare numerical solutions in the small- v case (Section 3.2, equations 20), the adiabatic case (Section 3.3, equations 22) and our original model in CP23. First, in Section 4.4.1 we use the same low metallicity donor $30 M_\odot$ as in CP23 that is adopted from Marchant et al. (2021). Our results will justify the usage of the analytical estimate in the optically thick regime (equation 32). Next, in Section 4.4.2 we illustrate the differences between our present approach and the standard approach on a $40 M_\odot$ low-metallicity donor in a supergiant stage. This donor is ideal for this purpose because it achieves high values of the Eddington ratio in the surface layers ($\Gamma_{\text{Edd}} > 0.5$), but does not cross into the super-Eddington regime. For completeness, we present in Appendix D comparison for a $1 M_\odot$ red giant showing that in this case radiation has little effect on \dot{M} , as expected.

Finally, we introduce the notation for the previous MT rate prescriptions. For Roche-lobe-underfilling donors, $R_d \leq R_L$, we will use the optically thin model of Jackson et al. (2017), which is based on Ritter (1988). We will refer to this MT rate by \dot{M}_J and the expression can be found in equation (C4). For a Roche-lobe-overfilling donor, $R_d \geq R_L$, we will use the optically thick model of Kolb & Ritter (1990). We will refer to this MT rate by \dot{M}_{KR} and the expression is in equation (C6). In some cases, we will also use the prescription introduced by Marchant et al. (2021), \dot{M}_M .

4.4.1 $30 M_\odot$ donor undergoing thermal time-scale mass transfer

We used a $30 M_\odot$ low-metallicity donor undergoing intensive thermal time-scale MT to a black hole, as was investigated by Marchant et al. (2021). The donor's initial metallicity is $Z = Z_\odot/10$, where $Z_\odot = 0.0142$ (Asplund et al. 2009) and where the relative metal mass fractions are from Grevesse & Sauval (1998). We take a model with a $7.5 M_\odot$ black hole and an initial period of 31.6 d. We recalculated the evolution using the full MT prescription \dot{M}_M and the same MESA version as in Marchant et al. (2021).

As in CP23, we first examine the binary near the end of the thermal time-scale MT phase at an age of 6.79 Myr, with a surface Eddington factor $\Gamma_{\text{Edd}} = 0.78$, donor mass $M_d = 14.0 M_\odot$, core helium abundance 0.36, relative radius excess $\delta R_d = 3.18 \times 10^{-2}$, and mass ratio $q = 1.85$. Here, $\delta R_d \equiv \Delta R_d/R_L$, where $\Delta R_d \equiv R_d - R_L$ is the radius excess, and $q \equiv M_d/M_a$ is the donor-to-accretor (black hole) mass ratio.

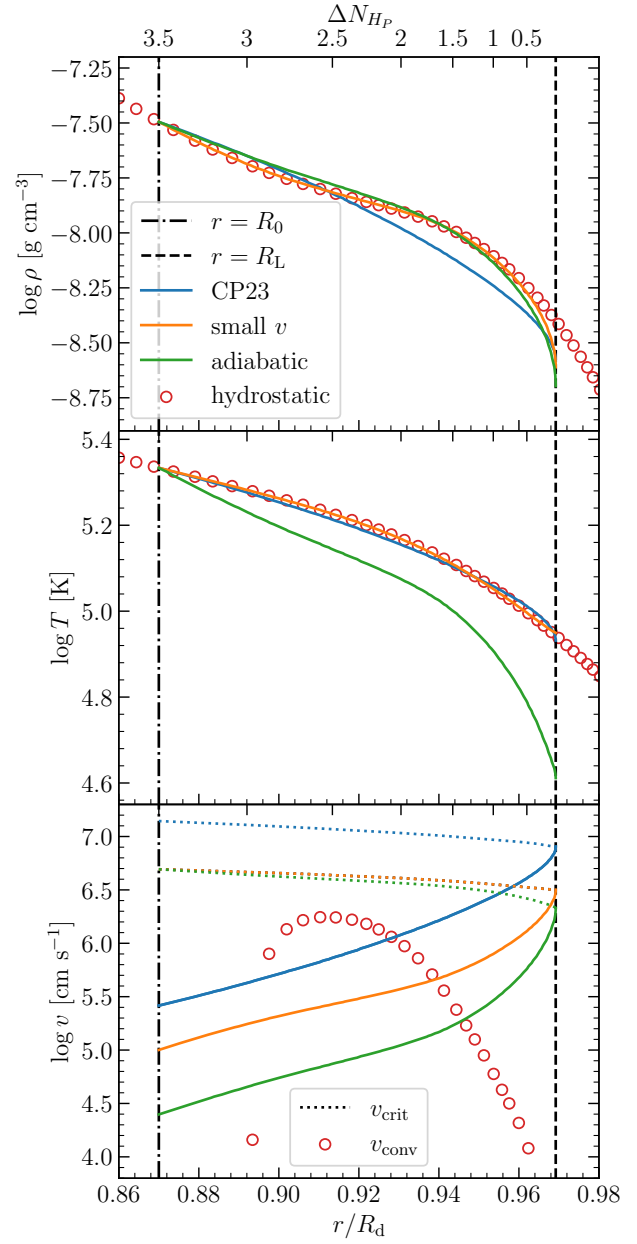


Figure 2. Comparison of density ρ , temperature T , and velocity v profiles for a $30 M_\odot$ low-metallicity star undergoing thermal time-scale MT (CP23), small- v case (Section 3.2), and adiabatic case (Section 3.3). We also show the underlying MESA hydrostatic density and temperature profiles and the value of convective velocity v_{conv} . The profiles are shown as functions of radius r going from the inner boundary at R_0 (that corresponds to x_0), to the outer boundary at R_L (the L1 point at x_1). The critical velocity v_{crit} , indicated by dotted lines, is reached at the critical point, L1. With the top x axis we indicate the distance to the critical point in units of pressure scale heights ΔN_{H_P} .

In Fig. 2, we compare the density, temperature, and velocity profiles for a fixed value of R_0 with the hydrostatic values from MESA. We find that the small- v case best matches the MESA hydrostatic profile, reproducing it well up to the vicinity of the L1 point, where the hydrostatic assumption $v \ll c_{T,\text{gas}}$ in MESA breaks down. The only potential source of discrepancy is convection, which is not included

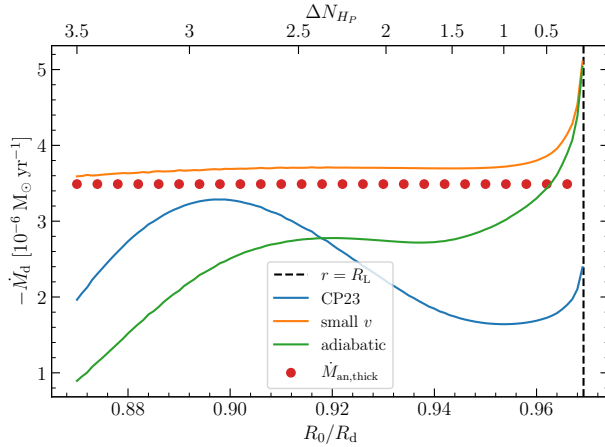


Figure 3. Comparison of the dependencies of the donor’s MT rate $-\dot{M}_d$ on R_0 for the same cases and donor star as in Fig. 2. We also show the analytical estimate $\dot{M}_{\text{an},\text{thick}}$ (equation 32). The outer fixed boundary at R_L is indicated as well as the distance between R_0 and R_L in units of pressure scale heights ΔN_{H_P} .

in our model. However, even though convective velocities v_{conv} exceed flow velocities locally, our model still captures the MESA profile accurately.

This agreement is also evident in Fig. 3, which shows the corresponding MT rates for different values of R_0 . Furthermore, we include the analytical estimate $\dot{M}_{\text{an},\text{thick}}$ (equation 32). We find that $\dot{M}_{\text{small},v}$ remains nearly constant up to the immediate vicinity of the L1 point ($\Delta N_{H_P} \lesssim 0.5$), however, it is not surprising that the model becomes inaccurate when R_0 is positioned too close to the critical point. The small deviations arise from convective effects, which are not included in our model.

In Fig. 3 we also see that the MT rates of CP23 and in the adiabatic case follow a similar trend, but the CP23 model gives a lower value of the MT rate, which we discuss in more detail in Section 4.5. The similarity of the trends is caused by the fact that the CP23 model is also adiabatic (in the sense that there is no energy exchange between gas and radiation), but it also includes the averaging of physical quantities over the L1 plane. Therefore, as the gas approaches L1, it cools down and its cross-section decreases, its potential energy decreases, and the difference is used to heat up the gas, as we can also see in the middle panel of Fig. 2.

In Fig. 4, we compare different MT rates throughout the evolution of the $30 M_\odot$ donor. First, we compare the small- v case with the analytical expression $\dot{M}_{\text{an},\text{thick}}$ (equation 32). We then compare the MT prescription of Kolb & Ritter (1990), \dot{M}_{KR} , with $\dot{M}_{\text{an},\text{thick}}$, followed by a comparison of the MT rate \dot{M}_M from Marchant et al. (2021) with the modified analytical expression

$$-\dot{M}_d \approx \dot{M}_{\text{an},\text{thick,tot}} \equiv \frac{1}{\sqrt{e}} \frac{2\pi}{\sqrt{BC}} \frac{\bar{P}^{3/2}}{\bar{\rho}^{1/2}} \Big|_{r=R_L}, \quad (40)$$

which modifies $\dot{M}_{\text{an},\text{thick}}$ by replacing P_{gas} with P and removing the super-Eddington boost. Finally, we compare $\dot{M}_{\text{an},\text{thick,tot}}$ with $\dot{M}_{\text{an},\text{thick}}$.

We find that the small- v case and $\dot{M}_{\text{an},\text{thick}}$ agree well throughout the evolution, with differences within $\sim 20\%$. When the inner boundary is significantly below the L1 point ($\Delta N_{H_P} \lesssim 1$), $\dot{M}_{\text{small},v}$ remains nearly independent of R_0 , the only free parameter in our model. The only exception occurs at the final point, where a small discrepancy

arises between the orange and green markers, likely due to convection, which is not included in our model. Here, v_{conv} increases to $\sim 10^7 \text{ cm s}^{-1}$ below the surface. This agreement supports the use of $\dot{M}_{\text{an},\text{thick}}$ (equation 32) as a benchmark for other MT prescriptions.

In the second panel, $\dot{M}_{\text{an},\text{thick}}$ agrees with \dot{M}_{KR} to within $\sim 20\%$, except at the final point, where $\dot{M}_{\text{an},\text{thick}}$ is approximately twice as large. In the third panel, $\dot{M}_{\text{an},\text{thick,tot}}$ matches \dot{M}_M within $\sim 10\%$, further justifying its use. Finally, the bottom panel shows that $\dot{M}_{\text{an},\text{thick}}$ is consistently about twice as low as $\dot{M}_{\text{an},\text{thick,tot}}$, which would impact binary evolution if used self-consistently instead of $\dot{M}_{\text{an},\text{thick,tot}}$ (\dot{M}_M). The effects would resemble those of evolving the binary with \dot{M}_{KR} (see the second panel of Fig. 4). For details, refer to Marchant et al. (2021), or see CP23, where we previously illustrated the impact of reducing the MT rate by a factor of a few. Therefore, we do not repeat this analysis here but discuss the implications in more detail in Section 6.

4.4.2 $40 M_\odot$ supergiant donor

Here, we use a single nonrotating star with an initial mass of $40 M_\odot$ and the same low metallicity as in Section 4.4.1. We evolve the star to an age of 5.30 Myr, when we obtain a supergiant with a core helium fraction of 0.64, mass $M_d = 38.2 M_\odot$, effective temperature $T_{\text{eff}} = 1.2 \times 10^4 \text{ K}$, radius $R_d = 190 R_\odot$, luminosity $L_d = 6.5 \times 10^5 L_\odot$, and Eddington ratio $\Gamma_{\text{Edd}} = 0.70$ at the surface.

In Fig. 5 we show the comparison of our new analytical estimates $\dot{M}_{\text{an},\text{thin}}$ (equation 36) and $\dot{M}_{\text{an},\text{thick}}$ (equation 32) with the standard model of optically-thin MT (Jackson et al. 2017, \dot{M}_J , equation C4) and optically-thick MT (Kolb & Ritter 1990, \dot{M}_{KR} , equation C6). Here, we measure the absolute radius excess ΔR_d in the units of the photosphere pressure scale height $H_{P,\text{ph}}$ defined as

$$H_{P,\text{ph}} \equiv \frac{P_{\text{ph}}}{\rho_{\text{ph}}} \frac{R_d^2}{GM_d}, \quad (41)$$

where P_{ph} is the photosphere pressure. We see that in the optically thin regime $\dot{M}_{\text{an},\text{thin}}$ is greater than \dot{M}_J due to the momentum boost from radiation that is included in our expression, and the relative difference is growing exponentially. In contrast, $\dot{M}_{\text{an},\text{thick}}$ is similar to \dot{M}_{KR} because the model of Kolb & Ritter (1990) integrates the total pressure (including P_{rad}) of the overflowing layers and therefore includes much of the radiation boost. We also confirm that $\dot{M}_{\text{an},\text{thin}} \approx \dot{M}_J$ and $\dot{M}_{\text{an},\text{thick}} \approx \dot{M}_{\text{KR}}$ for a gas pressure dominated envelope ($P_{\text{gas}} \gg P_{\text{rad}}$) on a solar-like donor on the red giant branch, see Appendix D.

4.5 Comparison to previous works

There are two main implications for sub-Eddington MT based on our results in this Section. First, for Roche-lobe-underfilling donors (optically thin case), the MT rate increases exponentially with the Eddington factor at the photosphere. This effect is not part of the existing prescriptions, but can be easily included by using equation (36). Second, for Roche-lobe-overfilling donors, the MT rate is very similar to existing prescriptions because the underlying hydrostatic stellar structure is already taking radiation pressure into account. Subsurface convective regions appear to have only minimal influence on the MT rate. In this regime, we provide a convenient expression (equations 32, 40) to evaluate the MT rate without the need to integrate the stellar structure or solve the hydrodynamic equations. The uncertainties arising from using this expression appear similar to the systematic differences between existing MT prescriptions (Fig. 4).

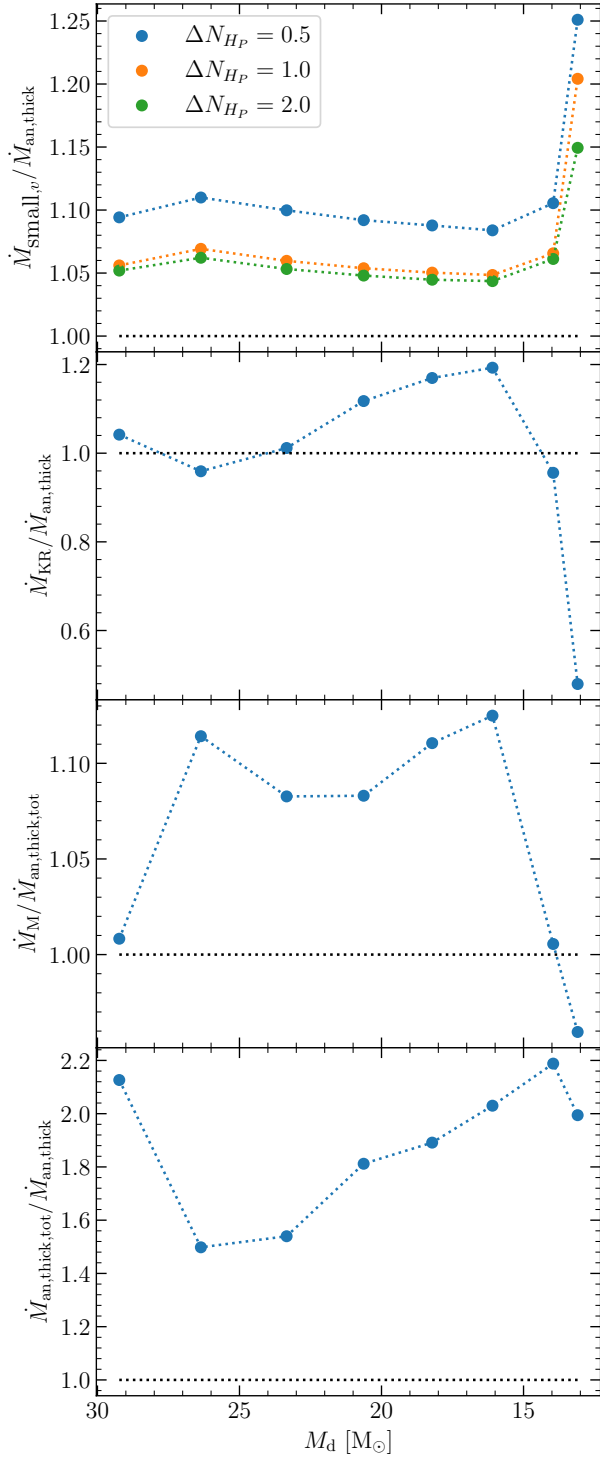


Figure 4. Comparison of different MT prescriptions throughout the evolution of originally $30M_{\odot}$ low-metallicity donor undergoing thermal time-scale MT (Section 4.4.1, Marchant et al. 2021). First panel: the small- v case (Section 3.2) for three different values of the distances between the inner and outer boundary in units of pressure scale heights ΔN_{H_P} vs. the analytical estimate $\dot{M}_{\text{an},\text{thick}}$ (equation 32). Second panel: the MT prescription introduced by Kolb & Ritter (1990), \dot{M}_{KR} vs. the analytical estimate $\dot{M}_{\text{an},\text{thick}}$. Third panel: the MT prescription introduced by Marchant et al. (2021), \dot{M}_M , vs. the analytical estimate $\dot{M}_{\text{an},\text{thick,tot}}$ (equation 40). Fourth panel: Comparison of the two analytical prescriptions $\dot{M}_{\text{an},\text{thick,tot}}$ vs. $\dot{M}_{\text{an},\text{thick}}$, throughout the evolution.

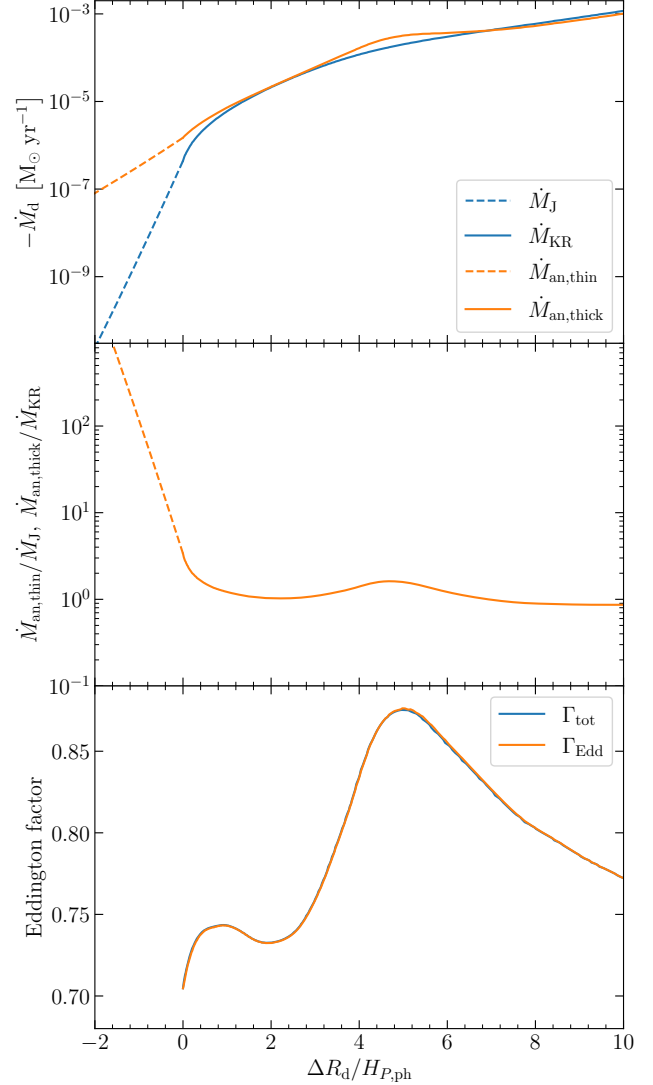


Figure 5. Comparison of our analytical MT prescription $\dot{M}_{\text{an},\text{thin}}$ and $\dot{M}_{\text{an},\text{thick}}$ with the optically thin prescription introduced by Jackson et al. (2017), \dot{M}_J , and the optically thick prescription introduced by Kolb & Ritter (1990), \dot{M}_{KR} . We also show the Eddington factors $\Gamma_{\text{tot}} = L/L_{\text{Edd}}$ and Γ_{Edd} (equation 28). The case shown is for an isolated originally $40M_{\odot}$ low-metallicity star in the supergiant stage.

We now compare the approach in this paper to our previous work in CP23. For convenience, we summarize the equations from CP23 in Appendix C. The greatest difference between these works comes from the fact that here we assume that all physical quantities are constant along Q and we use a physically motivated expression for Q (equations 30, 31), where Q is appropriately enlarged by a factor of $1/(1-\Gamma_{\text{Edd}})$. In contrast, in CP23 we assumed hydrostatic equilibrium in the yz -plane together with a polytropic EOS and averaged over the yz -plane. As a result, characteristic cross sections corresponding to density and pressure profiles, Q_ρ and Q_P , appeared in all equations. Moreover, CP23 had an extra term on the right-hand side of the energy equation (C1c) that is a consequence of the average of the Roche potential ϕ_R in the yz plane. The effects of this term can be understood by realizing that if the gas is farther from the x axis, its potential is greater. Consequently, if the cross section shrinks, the potential energy becomes lower, and this energy difference is used to

heat the gas. Thus, our original CP23 model is not strictly adiabatic but is adiabatic in the sense that there is no energy exchange between the gas and radiation.

In the present paper, we define two limiting cases: the small- v case that is inspired by the hydrostatic case (Section 3.2) and the adiabatic case with no energy exchange between gas and radiation and no extra term on the right-hand side of the energy equation (Section 3.3). The adiabatic case behaves similarly to the original ‘‘adiabatic’’ CP23 model with the difference that the adiabatic case gives a steeper temperature gradient resulting in a lower temperature at L1 and thus lower critical velocity v_{crit} and a lower value of the MT rate. Also, if x_0 approaches x_1 , the two cases obtain different Q and v_{crit} and consequently also different MT rates. Specifically, the adiabatic case obtains $Q \propto P_{\text{gas}}/\rho/(1 - \Gamma_{\text{Edd}}) \propto P/\rho$ and $v_{\text{crit}}^2 = P_{\text{gas}}/\rho$, while our original model had $Q \propto c_{T,\text{gas}}^2 \propto P_{\text{gas}}/\rho$ and $v_{\text{crit}}^2 \sim P/\rho$. Hence, the original model obtains a lower value of the MT rate even in this limiting case as $-\dot{M}_d \propto v_{\text{crit}} Q$. The small- v case and the adiabatic case obtain the same MT rate in the limit of $x_0 \rightarrow x_1$ because they predict the same Q and v_{crit} . This behavior is illustrated in Figs. 2 and 3.

5 SUPER-EDDINGTON MASS TRANSFER

We now analyze situations where the star exceeds the Eddington limit interior of the L1 point. We could still solve our equations with x_0 in a sub-Eddington region and define x_1 as the point where $\Gamma_{\text{Edd}} = 1$. However, super-Eddington flux can often be carried out by convection without any outflows. Outflows may only develop when convective efficiency diminishes and v_{conv} approaches the sound speed. In principle, our equations could be extended to include convective energy transport using, for example, the formalism of Kuhfuss (1986), where the outflow should naturally develop once convection is unable to carry the flux. However, studies of single nonrotating super-Eddington stars have shown that multidimensional effects fundamentally alter the structure of the relevant regions (e.g., Shaviv 2001b; Owocki et al. 2004; Jiang et al. 2015, 2018). This suggests that further refinements of our 1D model may be of limited value. Instead, we revisit some of the arguments constraining super-Eddington outflows in spherical symmetry and find that proximity to the L1 point may relax some of them. While our results are promising with respect to the potential for a super-Eddington MT boost, determining whether such outflows actually occur will ultimately require multidimensional time-dependent simulations.

5.1 Analytic theory

We need to consider three issues determining the viability of a super-Eddington boost to MT: (i) efficiency of convection for transferring the energy flux, (ii) properties of the super-Eddington MT boost such as the MT rate, and (iii) whether the flow satisfies the limits of photon tiring. The discussion of the first issue does not depend on the geometry and we can simply assume that convection becomes unable to carry the super-Eddington flux once the required velocities of convective eddies v_{conv} exceed the local sound speed, or alternatively when $L_d \gtrsim 4\pi r^2 \rho c_{T,\text{gas}}^3$.

For the discussion of the two remaining issues, we first outline the theory of super-Eddington outflows from spherically-symmetric stars presented by Owocki et al. (2004) and later revisited by Quataert et al. (2016) and Owocki et al. (2017), and then modify the results to the context of the L1 point. For $\Gamma_{\text{tot}} = L/L_{\text{Edd}} > 1$ and inefficient

convection, the entire luminosity can be carried by an outflow with velocity $v_{\text{out}} \gtrsim c_{T,\text{gas}}$ satisfying

$$L_d \sim 4\pi R_d^2 \rho v_{\text{out}}^3, \quad (42)$$

where we assume that the launching region with density ρ is located close to the surface R_d . This implies a spherically symmetric mass-loss rate of

$$\dot{M}_{\text{out}} = 4\pi R_d^2 \rho v_{\text{out}} \sim \frac{L_d}{v_{\text{out}}^2}. \quad (43)$$

The outflow velocity v_{out} depends on Γ_{tot} , but part of the luminosity can still be transported by radiation, making the estimate of v_{out} in equation (42) effectively an upper limit.

The super-Eddington outflow, however, should not exceed the photon-tiring limit

$$\dot{M}_{\text{tir}} \equiv \alpha_{\text{tir}} \frac{L_d}{GM_d/R_d} = \alpha_{\text{tir}} \frac{2L_d}{v_{\text{esc}}^2}, \quad (44)$$

where $\alpha_{\text{tir}} = 1 - 1/\Gamma_{\text{tot}}$ is the efficiency parameter of photon tiring (Owocki et al. 2017). If $\dot{M}_{\text{out}} \gtrsim \dot{M}_{\text{tir}}$, the outflow should just stall. The condition for an outflow to form is thus

$$\beta_{\text{SE}} \equiv \frac{1}{2\alpha_{\text{tir}}} \frac{v_{\text{esc}}^2}{v_{\text{out}}^2} \lesssim 1. \quad (45)$$

Since $v_{\text{esc}} \gg c_{T,\text{gas}} \sim v_{\text{out}}$ and $\alpha_{\text{tir}} < 1$, this condition is not satisfied and the spherically-symmetric outflow should always stall.

Models based on the porosity length formalism suggest that the maximum achievable mass loss rate is proportional to the gravitational scale height (e.g. Owocki et al. 2004), and thus inversely proportional to effective gravity $g_{\text{eff}} \propto \nabla\phi_R$ in a Roche model, where $\nabla\phi_R \rightarrow 0$ close to L1. Consequently, we assume that if an outflow occurs from a star nearly filling its Roche lobe and possessing a super-Eddington, convectively inefficient subsurface zone, it will primarily flow through the nozzle surrounding L1 at a rate $\dot{M}_{\text{out,L1}}$. The detailed steps needed for the modifications from spherical symmetry to the vicinity of L1 are described in Appendix E. In summary, we take into account the limited extent of the nozzle by multiplying \dot{M} by $Q/(4\pi R_d^2) \sim c_{T,\text{gas}}^2/v_{\text{esc}}^2$, and differences in potential proportional to v_{esc}^2 are multiplied by δR_L . These modifications give

$$\dot{M}_{\text{out,L1}} \equiv \frac{Q}{4\pi R_d^2} \dot{M}_{\text{out}} = \frac{c_{T,\text{gas}}^2}{v_{\text{esc}}^2} \frac{L_d}{v_{\text{out}}^2}, \quad (46)$$

$$\dot{M}_{\text{tir,L1}} \equiv \alpha_{\text{tir}} \frac{L_N}{\bar{\phi}(R_L) - \bar{\phi}(R_{\text{SE}})} = \alpha_{\text{tir}} \frac{c_{T,\text{gas}}^2}{v_{\text{esc}}^2 \delta R_L} \frac{2L_d}{v_{\text{esc}}^2}, \quad (47)$$

where R_{SE} is a radius inside the donor where $\Gamma_{\text{Edd}} > 1$ and the condition for the outflow not to stall reads

$$\beta_{\text{SE,L1}} = \frac{1}{2\alpha_{\text{tir}}} \frac{v_{\text{esc}}^2}{v_{\text{out}}^2} \delta R_L = \beta_{\text{SE}} \delta R_L \lesssim 1. \quad (48)$$

Since δR_L can be made arbitrarily small by positioning the super-Eddington layer very close to the Roche lobe, this modified condition can be satisfied and the super-Eddington outflow will not be limited by photon tiring. In such a case, a super-Eddington outflow with velocity v_{out} and MT rate $-\dot{M}_d \sim \dot{M}_{\text{out,L1}}$ forms through the L1 point. Let us note here that the outflow rate $\dot{M}_{\text{out,L1}}$ does not depend on the distance from the L1 point, but only on the properties of the donor. The condition (48) is satisfied close to the L1 point because the photon-tiring limit $\dot{M}_{\text{out,L1}}$ increases as the super-Eddington layer approaches the L1 point.

Quataert et al. (2016) presented a different formulation of the photon tiring limit. They argued that equation (42) is valid when

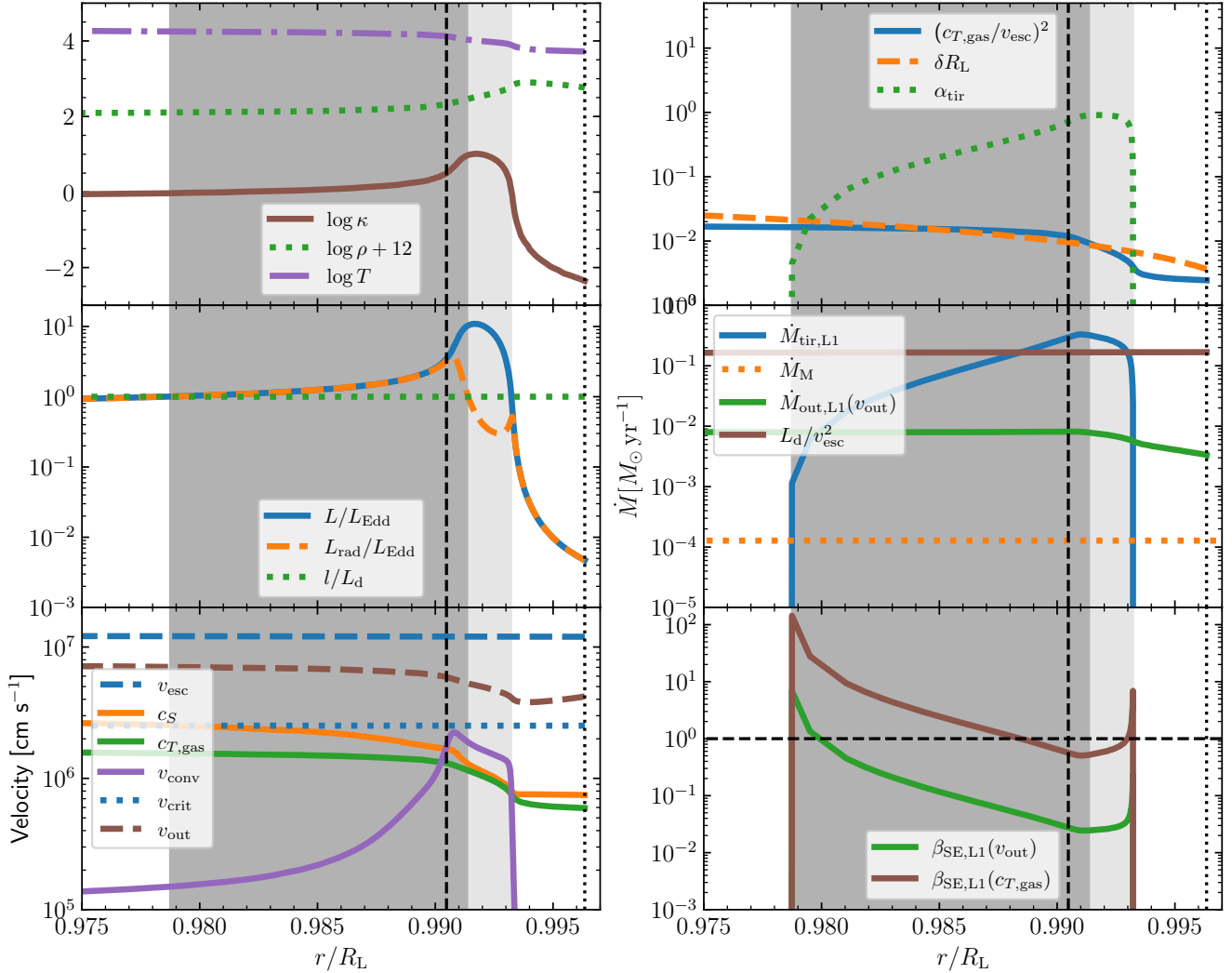


Figure 6. Radial profiles of key quantities for an initially $30 M_{\odot}$ low-metallicity star during the super-Eddington MT boost at $t = 6.972$ Myr, when the donor has $M_d = 28.57 M_{\odot}$, $T_{\text{eff}} = 5255$ K, $L_d = 3.96 \times 10^5 L_{\odot}$, and $R_d = 759 R_{\odot}$. Upper left panel shows profiles of density, temperature, and opacity. Middle left panel shows Eddington ratios of total (L) and radiative (L_{rad}) luminosities and relative luminosity profile l/L_d . Bottom left panel shows values of escape velocity v_{esc} , sound speeds c_s and $c_{T,\text{gas}}$, convective velocity reported by the MLT modules in MESA v_{conv} , outflow velocity v_{out} (equation 42), and the critical velocity v_{crit} of Quataert et al. (2016). Upper right panel displays the estimate for L1 nozzle area $(c_{T,\text{gas}}/v_{\text{esc}})^2$, relative distance to the L1 point δR_{L} , and efficiency parameter of photon tiring α_{tir} . Middle right panel shows estimates of L1 MT rates based on super-Eddington boosted MT $\dot{M}_{\text{out},\text{L1}}$ (equation 46), a more pessimistic estimate with v_{out} replaced with $c_{T,\text{gas}}$, L_d/v_{esc}^2 , and the prediction of Marchant et al. (2021) \dot{M}_M . In addition, we show also the photon tiring limit $\dot{M}_{\text{tir},\text{L1}}$ (equation 47). Bottom right panel shows the condition for super-Eddington boost $\beta_{\text{SE,L1}}$ evaluated using v_{out} or $c_{T,\text{gas}}$ (equation 48). In all panels, light and dark shading marks super-Eddington regions based on L and L_{rad} , vertical dashed line shows the interior most point where $v_{\text{conv}} > c_s$, and the vertical dotted line indicates the position of the photosphere.

the critical velocity of the outflow, $v_{\text{crit}} \sim (GL_d)^{1/5}$, exceeds the local escape velocity modified by a factor taking into account the structure of the surrounding envelope. In the vicinity of the L1 point, their condition reads $v_{\text{crit}} \gtrsim v_{\text{esc}} \delta R_{\text{L}}^{1/2}$. We show this condition in the figures that illustrate the super-Eddington MT boost, but we do not find significant differences in the outcomes when compared to equation (48).

5.2 Application to a realistic star

The higher the photon-tiring limit $\dot{M}_{\text{tir},\text{L1}}$ (equation 47), the easier it is to form an outflow through the L1 point. Therefore, we want the Eddington factor Γ_{Edd} to be as high as possible in the super-

Eddington layer. The maximum Eddington factor inside stars was investigated by Sanyal et al. (2015), who analyzed massive stars at LMC metallicity. They found that the local Eddington factor can exceed seven due to the hydrogen opacity bump near the photosphere in stars with effective temperatures around 5500 K (see their fig. 3). Fortunately, a similar situation arises in the $30 M_{\odot}$ low-metallicity donor studied by Marchant et al. (2021).

Thus, to illustrate the super-Eddington MT boost we use the same $30 M_{\odot}$ low-metallicity donor as in Sec. 4.4.1 but this time in a binary with an initial $4.5 M_{\odot}$ black hole and initial orbital period of 1000 days. As before, we recalculated the evolution using the full MT prescription \dot{M}_M and the same MESA version as in Marchant et al. (2021). Our first goal is to investigate how to evaluate the conditions

for a super-Eddington MT boost on realistic stellar profiles. In Fig. 6, we show radial profiles of a number of relevant quantities near the outer edge of the stellar envelope at a moment, when the donor still underfills its Roche lobe. Donor radius is $R_d = 0.9963R_L$ (vertical dotted line in Fig. 6), which means that the relative radius excess is $\delta R_d = -0.00365$. We see that the super-Eddington layer reaches $\Gamma_{\text{tot}} \gtrsim 10$, occurs in the hydrogen recombination zone, and is accompanied by a density inversion (upper left panel). The rapid decline of Γ_{tot} near the photosphere is caused by the sharp drop in opacity (upper left panel), while the luminosity L remains constant throughout the donor's envelope (middle left panel). We find that simple estimates of the convective energy flux differ sufficiently from the results of mixing length theory (MLT) of convection implemented in MESA and are not useful. Instead, we diagnose the inefficiency of convection by comparing the v_{conv} reported by MLT with the local sound speed (lower left panel), finding that convection is inefficient in a region $0.990 \lesssim r/R_L \lesssim 0.993$. This result is insensitive to the use of c_S or $c_{T,\text{gas}}$ for comparison purposes. The lower left panel of Fig. 6 also shows v_{crit} . Near the L1 point, we find that the relevant quantities for the Quataert et al. (2016) version of the photon tiring are $v_{\text{crit}} \approx 25 \text{ km s}^{-1}$, $v_{\text{esc}} \approx 120 \text{ km s}^{-1}$, and $\delta R_L^{1/2} \approx 0.1$ implying that the requirement is satisfied and equation (42) can be used to find v_{out} . Our results indicate that v_{out} exceeds the local sound speed by a factor of 3–4, but remains smaller than v_{esc} . The middle right panel of Fig. 6 displays \dot{M} near L1 corresponding to the MT flow and the photon tiring limit. The shape of \dot{M}_{tir} is mostly determined by a_{tir} (upper right panel). We find that $\dot{M}_{\text{out,L1}} < \dot{M}_{\text{tir,L1}}$ and correspondingly $\beta_{\text{SE,L1}} < 1$ in a significant range of r (bottom right panel). Since there is some ambiguity about the correct value of v_{out} , we also show an estimate of $\dot{M} = (c_{T,\text{gas}}/v_{\text{esc}})^2 L_d/c_{T,\text{gas}}^2 = L_d/v_{\text{esc}}^2$ and modified $\beta_{\text{SE,L1}}(c_{T,\text{gas}})$, where v_{out} is replaced with $c_{T,\text{gas}}$ in equation (48). Even in this more pessimistic case, the implied MT rate does not exceed the photon tiring limit. While in this case the outflow condition is satisfied later in the evolution (only about 700 years before Roche-lobe overflow), the implied MT rates are higher leading to a higher total mass lost.

To summarize Fig. 6, we find that at this point in evolution the donor is underfilling its Roche lobe, but the super-Eddington flux in the subsurface layer probably leads to MT through L1 with a rate of around $10^{-2} \text{ M}_\odot \text{ yr}^{-1}$, which is significantly lower than the photon tiring limit near L1 but also significantly higher than the MT rate of about $10^{-4} \text{ M}_\odot \text{ yr}^{-1}$ calculated using the traditional approach (Marchant et al. 2021).

We now proceed to evaluate the time dependence of the super-Eddington MT boost and its importance for binary evolution by post-processing the evolution calculated using the traditional MT model without the super-Eddington boost. This serves to illustrate the possible outcomes rather than provide quantitative predictions, which would require a self-consistent evolutionary calculation. In Fig. 7, we show the time evolution of relevant quantities a few thousand years before and after Roche-lobe overflow, which occurs at about 6.973 Myr and which we set as $t = 0$. We find that the donor with the super-Eddington subsurface layer expands and the convection efficiency decreases until about $t = -12 \text{ kyr}$ when $v_{\text{conv}} > c_S$. Shortly after, at $t = -11 \text{ kyr}$, $\beta_{\text{SE,L1}}$ decreases below unity, and the donor should begin experiencing super-Eddington boosted MT. The implied MT rates of 10^{-3} to $10^{-2} \text{ M}_\odot \text{ yr}^{-1}$ dramatically exceed the traditional optically thin MT rates or the donor's mass loss due to stellar winds (Marchant et al. 2021). Since on surface $\Gamma_{\text{tot}} \lesssim 0.1$, the Eddington boost to the optically thin MT rate discussed in Section 4.3.1 is not strong. For the final 1 kyr before Roche-lobe overflow, the traditionally calculated MT rate quickly increases and approaches

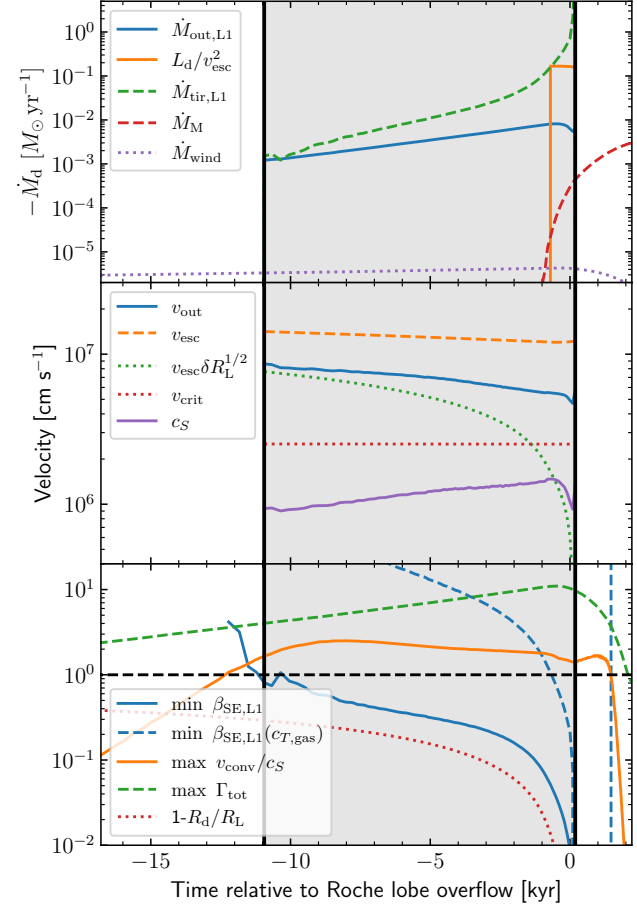


Figure 7. Time evolution of donor properties illustrating super-Eddington boosted MT on an initially 30 M_\odot star in a binary with a 4.5 M_\odot black hole. Top panel shows estimates of L1 MT rates $\dot{M}_{\text{out,L1}}$ (equation 46), \dot{M}_M (Marchant et al. 2021), and a more pessimistic estimate for super-Eddington MT $\dot{M} = L_d/v_{\text{esc}}^2$, as well as photon tiring limit $\dot{M}_{\text{tir,L1}}$ and wind mass loss from the donor \dot{M}_{wind} . Middle panel shows the evolution of relevant velocities v_{out} , v_{esc} , v_{crit} , and c_S . Bottom panel shows time evolution of the minimum of $\beta_{\text{SE,L1}}$, maximum of v_{conv}/c_S , and maximum of $\Gamma_{\text{tot}} = L/L_{\text{Edd}}$ evaluated over the subsurface region that could drive super-Eddington MT, and the relative Roche-lobe-filling factor of the star $1 - R_d/R_L$.

$10^{-3} \text{ M}_\odot \text{ yr}^{-1}$. At $t = 0$, the super-Eddington MT boost formally ends because the driving region moves outside the L1 point.

By integrating \dot{M}_d , we find that the total mass lost from the donor due to the super-Eddington MT exceeds 10 M_\odot . We obtain even higher numbers for the more pessimistic case when $v_{\text{out}} = c_{T,\text{gas}}$ or similar numbers even when we restrict the super-Eddington MT to the final 1 kyr before Roche-lobe overflow when $v_{\text{crit}} > v_{\text{esc}}\delta R_L^{1/2}$. These numbers are clearly an artifact of not evolving the binary self-consistently. We performed preliminary MESA simulations with the super-Eddington boost included (Hadač, Cehula, Pejcha, in preparation) and found that the star responds to pre-Roche overflow mass loss similarly to standard mass transfer, leading to overall similar evolution, however, the timing and observable signatures of the mass loss are different.

6 SUMMARY AND DISCUSSION

In this paper, we investigated the effect of radiation pressure on MT in binary stars. Starting from 3D time-steady radiation hydrodynamic equations in the flux-limited diffusion approximation (equations 1), we constructed 1D equations describing the flow near the L1 nozzle (equations 11). Using the von Zeipel theorem (Section 2.3), we defined several simplified cases in the limit of small velocities and optically thick regions (Section 3), where the flow is parameterized by the Eddington parameter Γ_{Edd} and the critical point occurs either at the L1 point or at $\Gamma_{\text{Edd}} = 1$. For sub-Eddington donors, $\Gamma_{\text{Edd}} < 1$, we were able to find several analytic estimates and algebraic solutions (Section 4.2 and 4.3) as well as numerically solve the equations in the context of massive low-metallicity donor (Section 4.4). For donors with a super-Eddington layer below the surface, we reformulated the limitations for outflows posed by convective efficiency and photon tiring and applied the theory to a binary evolution trajectory (Section 5). Our results can be summarized as follows.

- If the donor envelope is dominated by gas pressure, $P_{\text{gas}} \gg P_{\text{rad}}$ or equivalently $\Gamma_{\text{Edd}} \ll 1$, our model predicts a MT rate comparable to standard models by Jackson et al. (2017) and Kolb & Ritter (1990) in the optically thin and thick regimes, respectively. This is illustrated for a solar-like donor on the red giant branch in Fig. D1.
- If the donor envelope is dominated by radiation pressure, $P_{\text{rad}} \gg P_{\text{gas}}$ and $\Gamma_{\text{Edd}} \lesssim 1$, our optically thick rates are comparable to predictions of Kolb & Ritter (1990) and later works based on similar assumptions (Fig. 5). The reason is that radiation pressure is already accounted for in the hydrostatic stellar structure used as input in the existing models. However, for Roche-lobe-underfilling donors, our optically thin MT rates are significantly higher than the predictions of previous models of Ritter (1988) or Jackson et al. (2017) (Fig. 5). The increase in the MT rate is exponential in $1 - \Gamma_{\text{Edd}}$ and the effect can be included by a simple modification of existing prescriptions (equation 36).
- We derived an analytic approximation for the optically thick MT rate, which is based only on the quantities at the L1 point (equation 32). We verified that this approximation differs from numerical solutions by factors similar to the spread among existing MT models (Figs. 3 and 4).
- Super-Eddington convectively inefficient subsurface layers in single non-rotating donors lead to envelope inflation and density inversions, but should not develop super-Eddington outflows, because the implied mass-loss rates exceed the photon tiring limit (Owocki et al. 2004). In a binary system, the L1 point effectively brings the gravitational potential infinity much closer to the super-Eddington layer and effectively increases the photon tiring limit (equation 48). As a result, a super-Eddington-boosted MT could occur (Fig. 6). By postprocessing a binary evolutionary trajectory, we proposed that super-Eddington-boosted MT can occur before the donor overfills its Roche lobe and that MT rates reach $\gtrsim 10^{-2} M_{\odot} \text{ yr}^{-1}$ (Fig. 7). Consequently, this new mode of MT can fundamentally alter the evolutionary trajectories of massive binaries.

6.1 Implications

We have identified two new effects of radiation pressure on MT: the exponential increase in the optically thin MT rate for donors with a high but sub-Eddington surface Γ_{Edd} and the circumvention of the photon tiring limit in donors possessing super-Eddington convectively inefficient subsurface layers. The importance of the increased optically thin MT rate for binary evolution is likely limited, because although the rates are much higher than traditionally assumed, they

are still significantly lower than MT rates for Roche-lobe-overflowing donors or the mass lost from a massive donor by stellar winds. Moreover, the details of MT via the L1 point or the precise value of the Roche-lobe radius are not crucial for binary evolution, provided that the MT is stable and the long-term evolution is driven by other factors such as the nuclear or thermal timescale of the donor, as already pointed out by Paczyński (1971). In such cases, it is more important to consider mass and angular momentum loss from the binary.

Indeed, the enhanced optically thin rate could be important for donors undergoing wind Roche-lobe overflow and for the stability of massive contact binaries, which are already close to overflowing their outer Lagrangian points (L2 and L3). If substantial mass is lost through L2/L3 via an optically thin outflow analogous to a similar process near L1, it would carry away angular momentum, causing the binary to shrink. If this effect is strong enough, it could destabilize the contact binary, potentially leading to a runaway merger with consequences similar to what was observed in a low-mass merger V1309 Sco (e.g., Tylenda et al. 2011; Pejcha 2014; Pejcha et al. 2017). To assess this impact, future simulations should incorporate our MT model at the L2/L3 points.

The consequences of the potential super-Eddington MT boost in donors with a convectively inefficient subsurface layer are far-reaching. In Fig. 7, we only illustrate the possible effects by post-processing a binary evolution trajectory. Although the quantitative details are unreliable, we can still deduce general features that are likely valid. First, the super-Eddington MT boost can occur tens of kyr before the donor formally overflows its Roche lobe. The initial growth timescale of $\dot{M}_{\text{out},\text{L1}}$ is difficult to assess from the post-processed run, but the behavior of $\beta_{\text{SE,L1}}$ in Fig. 7 suggests that it is probably around a thousand years and possibly even less. The super-Eddington boost in Fig. 7 formally ends when the driving region moves beyond the L1 point, which becomes the innermost critical point of the outflow and the physical conditions at this point will determine \dot{M}_{d} (equation 6). It is reassuring that at $t = 0$, \dot{M}_{M} is not too different from $\dot{M}_{\text{out},\text{L1}}$. At $t > 0$, the effects of radiation pressure will likely affect the outflow velocity, which could become noticeably higher than the sound speed at L1.

The total amount of mass transferred during the super-Eddington boost depends on how the donor structure responds to this type of mass loss. We can imagine two scenarios. First, the super-Eddington MT simply adds to the traditional MT rate. The effective outcome of this could be simply that the Roche-lobe overflow occurs earlier than traditionally predicted, but the ultimate fate of the binary remains unaffected. Alternatively, if the mass transfer is already unstable and a hydrostatic structure can no longer be maintained in the outer layers, this additional boost could further accelerate the instability.

Second, the high $\dot{M}_{\text{out},\text{L1}}$ induces a strong response in the donor and the super-Eddington convectively inefficient layer disappears and the donor shrinks. The super-Eddington layer could reconstitute again, leading to expansion and repeating of the super-Eddington-boosted MT. In such a case, the donor might completely avoid overfilling its Roche lobe, and the binary evolution would be significantly altered. However, it is not clear how much different the ultimate fate of the binary would be.

This last scenario motivates further speculation on the cause of LBV outbursts. LBVs are hot, highly luminous massive stars that undergo large, quasi-periodic variations in brightness, radius, and photospheric temperature on timescales of years to decades, often accompanied by episodes of enhanced mass loss (Smith 2014). The connection between these eruptions and super-Eddington outflows has a long history (e.g., Smith & Owocki 2006), but it has not been clear what triggers the enhanced super-Eddington state.

A single-star scenario was recently proposed by [Grassitelli et al. \(2021\)](#). In addition to an inflated envelope close to the Eddington limit, they required two additional conditions to trigger the bursting activity: first, a temperature range in which decreasing opacities do not lead to an accelerating outflow; and second, a mass-loss rate that increases with decreasing temperature.

Our results in Fig. 7 might lead to a binary scenario for LBV outbursts. In addition to a super-Eddington, convectively inefficient subsurface layer, we also require this layer to be sufficiently close to the L1 point. When it is far from L1 and unable to drive an outflow due to photon tiring, it becomes subject to instabilities leading to up and down flows as well as small eruptions (e.g., [Owocki et al. 2004](#); [Jiang et al. 2015, 2018](#)). Once the donor slowly expands sufficiently close to the L1 point, the photon tiring limit is relaxed and the donor is able to drive an outflow through the L1 nozzle. Envelope instabilities are likely to make this process manifest as a series of distinct irregular bursts rather than a smooth outflow. The expected mass-transfer/outflow rates are consistent with what was inferred for LBV outbursts ([Smith 2014](#)). Depending on how the donor responds to this type of mass loss, there might be multiple phases of activity separated by inactive periods during which the driving region in the donor reconstitutes. In general, the donor might lose up to several M_{\odot} of material before the conditions for the outflow are no longer satisfied.

At first sight, such a scenario might seem extremely unlikely to occur. In this paragraph, we argue that this is not necessarily the case. If we evolve the $30 M_{\odot}$ low-metallicity donor from Sec. 5.2 as a single star, the super-Eddington and convectively inefficient subsurface layer is present for R_d/R_{\odot} between roughly 540 and 910. Assuming that the donor is in a binary, Keplerian orbit, and adopting the simple approximation for the Roche-lobe radius from [Paczynski \(1971\)](#), $R_L/a = 0.46[q/(1+q)]^{1/3}$, we obtain the following expression for the binary orbital period: $P_{\text{orb}} = 20\sqrt{R_L^3/GM_d} = 2.3 \text{ yr } R_{L,540}^{3/2} M_{d,30}^{-1/2}$, where $R_{L,540} = R_L/540 R_{\odot}$ and $M_{d,30} = M_d/30 M_{\odot}$. This expression does not depend on the binary mass ratio. Thus, if the $30 M_{\odot}$ low-metallicity donor resides in a binary with an orbital period between roughly 2.3 and 5.1 years, it should overflow its Roche lobe while possessing a super-Eddington, convectively inefficient subsurface layer, and a super-Eddington MT boost could occur. Given that most massive stars are in binaries (e.g., [Sana et al. 2012](#)), these numbers already suggest that such a scenario might not be extremely rare.

The diversity of outcomes of this binary scenario for LBV outbursts can be further increased by considering super-Eddington layers due to hydrogen, helium, or iron ionization, accretion onto the companion, which might be a compact object able to accelerate part of the material to high velocities, or eccentric passages of the companion, where the effective L1 point passes close to the surface only temporarily. All of these issues are nontrivially mapped on the properties of the initial conditions of binary components and their orbit. However, this scenario cannot possibly explain all LBV outbursts. For example, since the driving mechanism ultimate relies on stellar photons, the kinetic energy of the ejected material is limited by the energy radiated by the star, which is violated in the brightest LBV eruptions such as η Car ([Smith et al. 2011](#)).

6.2 Limitations and future work

We now discuss several limitations of our work and how we can improve our results in the future. The key assumption in our model is the von Zeipel theorem. Although this theorem is valid in stellar

interiors and for slowly rotating stars, it becomes less reliable near the stellar surface and Lagrangian points. Moreover, it is inherently inconsistent. In a stationary system where the radiative flux governs energy transport, energy conservation dictates a divergence-free flux (equations 1d, 1e). However, the assumption of proportionality between radiative flux and effective gravity (equation 16) implies the existence of the Poisson equation in the donor envelope, $\Delta\phi_R = 0$, in regions where $L(\phi_R) \approx \text{const.}$ and $M(\phi_R) \approx \text{const.}$ However, in reality, $\Delta\phi_R = -2\omega^2$, where ω is the binary orbital frequency. This inconsistency was resolved in 2D by [Espinosa Lara & Rieutord \(2011\)](#), which suggests a promising avenue for adopting their approach along the binary axis and for further generalization to 3D.

Another simplification of our 1D approach is the neglect of circulation (due to the one-dimensionality of the method) and, more importantly, the neglect of the Coriolis force. Recently, [Ryu et al. \(2025\)](#) performed 3D hydrodynamical simulations of MT through the L1 point, including the Coriolis force and assuming an ideal-gas EOS. They found that the Coriolis force affects the stream morphology by reducing the stream's cross-section and shifting its origin to the donor's trailing side. However, the resulting MT rates were only mildly suppressed relative to analytic predictions, within a factor of 2 at the L1 point. Without the Coriolis force, their results resemble our nozzle picture and agree with analytic prescriptions to within 5 percent. This suggests that including the Coriolis force in our model could mildly reduce the MT rate (by up to a factor of a few), but this effect should remain subdominant compared to, for example, the super-Eddington MT boost discussed in this work.

Our model for the super-Eddington MT boost in Section 5.1 assumes that the material will flow around L1 once the photon tiring limit becomes relaxed there. However, this is only a necessary but not sufficient condition. Instead, it is possible that lateral structuring or “porosity” will reduce the effective coupling between radiation and matter similar to what was previously argued for spherical stars (e.g., [Shaviv 2001a](#); [Owocki et al. 2004](#)), leading to a time-dependent but still nearly hydrostatic structure ([Jiang et al. 2015, 2018](#)).

There are several ways to further improve our model and understanding of MT in binaries in general. As a first step, 1D binary evolution models that include modifications to the optically thin MT and some prescription for the possible super-Eddington boost would be useful to investigate self-consistent response of the binary to these new modes of MT and to assess the effect on the outcomes of binary evolution and to connect to phenomena like LBV outbursts. However, the model of super-Eddington boost presented in Section 5 depends on several multidimensional radiation-hydrodynamic phenomena: von Zeipel theorem in Roche geometry, photon porosity of radiation pressure-dominated layers, inefficient convection, and the Coriolis force. Although effective 1D theories exist for each of these phenomena separately, capturing the mutual non-linear interactions in the context of some new 1D theory of super-Eddington MT boost is unlikely to be successful. Instead, future multidimensional, time-dependent radiation hydrodynamic simulations of MT through L1 are essential to test the validity of the simple model presented here and to further clarify the flow geometry, MT rate, and response to the super-Eddington condition (e.g., [Jiang et al. 2015, 2018](#); [Dickson 2024](#); [Ryu et al. 2025](#)). Given the difficulty of capturing 3D phenomena with 1D models, the relatively small but noticeable differences in the existing 1D MT prescriptions (Fig. 4) suggest that using a simple analytic prescription such as the one presented here in Section 4.2 might do as good a job as some more complicated 1D models.

ACKNOWLEDGEMENTS

JC thanks Damien Gagnier for useful comments. This research was supported by Czech Science Foundation Grant No. 24-11023S. JC also acknowledges support by the ETag grant PRG2159 during manuscript revision.

DATA AVAILABILITY

The data underlying this article will be shared on reasonable request to the corresponding author.

REFERENCES

- Alme M. L., Wilson J. R., 1973, *ApJ*, **186**, 1015
 Asplund M., Grevesse N., Sauval A. J., Scott P., 2009, *ARA&A*, **47**, 481
 Begelman M. C., 2001, *ApJ*, **551**, 897
 Belczynski K., Kalogera V., Bulik T., 2002, *ApJ*, **572**, 407
 Calderón D., Pejcha O., Duffell P. C., 2021, *MNRAS*, **507**, 1092
 Cehula J., Pejcha O., 2023, *MNRAS*, **524**, 471
 Chabrier G., Mazevert S., Soubiran F., 2019, *ApJ*, **872**, 51
 Dickson D., 2024, *ApJ*, **975**, 130
 Eggleton P. P., 1983, *ApJ*, **268**, 368
 Espinosa Lara F., Rieutord M., 2011, *A&A*, **533**, A43
 Fabry M., Marchant P., Sana H., 2022, *A&A*, **661**, A123
 Fabry M., Marchant P., Langer N., Sana H., 2023, *A&A*, **672**, A175
 Glatzel W., Kiriakidis M., 1993, *MNRAS*, **263**, 375
 Gräfener G., Vink J. S., de Koter A., Langer N., 2011, *A&A*, **535**, A56
 Grassitelli L., Langer N., Mackey J., Gräfener G., Grin N. J., Sander A. A. C., Vink J. S., 2021, *A&A*, **647**, A99
 Grevesse N., Sauval A. J., 1998, *Space Sci. Rev.*, **85**, 161
 Heger A., Langer N., 2000, *ApJ*, **544**, 1016
 Irwin A. W., 2008, FreeEOS, <http://freeeos.sourceforge.net/>
 Jackson B., Arras P., Penev K., Peacock S., Marchant P., 2017, *ApJ*, **835**, 145
 Jermyn A. S., Schwab J., Bauer E., Timmes F. X., Potekhin A. Y., 2021, *ApJ*, **913**, 72
 Jiang Y.-F., Cantiello M., Bildsten L., Quataert E., Blaes O., 2015, *ApJ*, **813**, 74
 Jiang Y.-F., Cantiello M., Bildsten L., Quataert E., Blaes O., Stone J., 2018, *Nature*, **561**, 498
 Joss P. C., Salpeter E. E., Ostriker J. P., 1973, *ApJ*, **181**, 429
 Kolb U., Ritter H., 1990, *A&A*, **236**, 385
 Krumholz M. R., Klein R. I., McKee C. F., Bolstad J., 2007, *ApJ*, **667**, 626
 Kuhfuss R., 1986, *A&A*, **160**, 116
 Lamers H. J. G. L. M., Cassinelli J. P., 1999, Introduction to Stellar Winds. Cambridge university press
 Lamers H. J. G. L. M., Fitzpatrick E. L., 1988, *ApJ*, **324**, 279
 Levermore C. D., Pomraning G. C., 1981, *ApJ*, **248**, 321
 Lubow S. H., Shu F. H., 1975, *ApJ*, **198**, 383
 Maeder A., 1987, *A&A*, **178**, 159
 Maeder A., Meynet G., 1987, *A&A*, **182**, 243
 Mahy L., et al., 2022, *A&A*, **657**, A4
 Mandel I., Broekgaarden F. S., 2022, *Living Reviews in Relativity*, **25**, 1
 Marchant P., Bodensteiner J., 2024, *ARA&A*, **62**, 21
 Marchant P., Pappas K. M. W., Gallegos-Garcia M., Berry C. P. L., Taam R. E., Kalogera V., Podsiadlowski P., 2021, *A&A*, **650**, A107
 Meyer F., Meyer-Hofmeister E., 1983, *A&A*, **121**, 29
 Mihalas D., 1969, *ApJ*, **156**, L155
 Mihalas D., Mihalas B. W., 1984, Foundations of radiation hydrodynamics. Oxford university press
 Moe M., Di Stefano R., 2017, *ApJS*, **230**, 15
 Owocki S. P., Gayley K. G., Shaviv N. J., 2004, *ApJ*, **616**, 525
 Owocki S. P., Townsend R. H. D., Quataert E., 2017, *MNRAS*, **472**, 3749
 Paczyński B., 1971, *ARA&A*, **9**, 183
 Paczynski B., 1976, in Structure and Evolution of Close Binary Systems.
- Paxton B., Bildsten L., Dotter A., Herwig F., Lesaffre P., Timmes F., 2011, *ApJS*, **192**, 3
 Paxton B., et al., 2013, *ApJS*, **208**, 4
 Paxton B., et al., 2015, *ApJS*, **220**, 15
 Paxton B., et al., 2018, *ApJS*, **234**, 34
 Paxton B., et al., 2019, *ApJS*, **243**, 10
 Pejcha O., 2014, *ApJ*, **788**, 22
 Pejcha O., Metzger B. D., Tyles J. G., Tomida K., 2017, *ApJ*, **850**, 59
 Potekhin A. Y., Chabrier G., 2010, *Contributions to Plasma Physics*, **50**, 82
 Press W. H., Flannery B. P., Teukolsky S. A., 2007, Numerical Recipes. The Art of Scientific Computing. Third Edition, 3rd edn. Cambridge university press
 Quataert E., Fernández R., Kasen D., Klion H., Paxton B., 2016, *MNRAS*, **458**, 1214
 Ritter H., 1988, *A&A*, **202**, 93
 Rogers F. J., Nayfonov A., 2002, *ApJ*, **576**, 1064
 Röpke F. K., De Marco O., 2023, *Living Reviews in Computational Astrophysics*, **9**, 2
 Ryu T., et al., 2025, *arXiv e-prints*, p. arXiv:2505.18255
 Sana H., et al., 2012, *Science*, **337**, 444
 Sanyal D., Grassitelli L., Langer N., Bestenlehner J. M., 2015, *A&A*, **580**, A20
 Saumon D., Chabrier G., van Horn H. M., 1995, *ApJS*, **99**, 713
 Shaviv N. J., 2001a, *MNRAS*, **326**, 126
 Shaviv N. J., 2001b, *ApJ*, **549**, 1093
 Shen R.-F., Nakar E., Piran T., 2016, *MNRAS*, **459**, 171
 Smith N., 2014, *ARA&A*, **52**, 487
 Smith N., Owocki S. P., 2006, *ApJ*, **645**, L45
 Smith N., Tombleson R., 2015, *MNRAS*, **447**, 598
 Smith N., Li W., Silverman J. M., Ganeshalingam M., Filippenko A. V., 2011, *MNRAS*, **415**, 773
 Tauris T. M., van den Heuvel E. P. J., 2023, Physics of Binary Star Evolution. From Stars to X-ray Binaries and Gravitational Wave Sources. Princeton University Press, doi:10.48550/arXiv.2305.09388
 Timmes F., 2021, Just a Module - Using MESA modules outside of MESA version 48b931, doi:10.5281/zenodo.4763740, <https://doi.org/10.5281/zenodo.4763740>
 Timmes F. X., Swesty F. D., 2000, *ApJS*, **126**, 501
 Tylerda R., et al., 2011, *A&A*, **528**, A114
 Vink J. S., de Koter A., Lamers H. J. G. L. M., 2000, *A&A*, **362**, 295
 Yoon S. C., Langer N., Norman C., 2006, *A&A*, **460**, 199
 Zhang W., Howell L., Almgren A., Burrows A., Bell J., 2011, *ApJS*, **196**, 20
 von Zeipel H., 1924, *MNRAS*, **84**, 665

APPENDIX A: DERIVATION OF 3D VELOCITY EQUATION

Here, we show the derivation of the velocity equation (6) for ideal gas EOS (equation 5) that is based on the set of radiation hydrodynamic equations (1). We also show the velocity equation (A8) for a general EOS. Performing the scalar product of \mathbf{v} and the momentum equation (1b), using the continuity equation (1a), and dividing the equation by ρ yields

$$\mathbf{v} \cdot \nabla \left(\frac{1}{2} |\mathbf{v}|^2 \right) + \frac{P_{\text{gas}}}{\rho} \mathbf{v} \cdot \nabla \ln P_{\text{gas}} + \frac{\lambda}{\rho} \mathbf{v} \cdot \nabla E_{\text{rad}} = -\mathbf{v} \cdot \nabla \phi_{\text{R}}. \quad (\text{A1})$$

Taking the energy equation (1c), using the continuity equation (1a), the definition of ϵ^* , see equation (2), dividing the equation by ρ and subtracting equation (A1) gives

$$\epsilon_{\text{gas}} \mathbf{v} \cdot \nabla \ln \epsilon_{\text{gas}} - \frac{P_{\text{gas}}}{\rho} \mathbf{v} \cdot \nabla \ln \rho = -c \kappa_{\text{P}} \left(aT^4 - E_{\text{rad}}^{(0)} \right). \quad (\text{A2})$$

Now, let us define useful thermodynamic quantities as follows

$$\chi_{\rho,\text{gas}} \equiv \frac{\partial \ln P_{\text{gas}}}{\partial \ln \rho} \Big|_T, \quad \chi_{T,\text{gas}} \equiv \frac{\partial \ln P_{\text{gas}}}{\partial \ln T} \Big|_{\rho}, \quad \psi_{\rho,\text{gas}} \equiv \frac{\partial \ln \epsilon_{\text{gas}}}{\partial \ln \rho} \Big|_T, \quad \psi_{T,\text{gas}} \equiv \frac{\partial \ln \epsilon_{\text{gas}}}{\partial \ln T} \Big|_{\rho}. \quad (\text{A3})$$

Using the above definition for the energy equation (A2) and rewriting it yields

$$\mathbf{v} \cdot \nabla \ln T = \frac{1}{\psi_{T,\text{gas}} \epsilon_{\text{gas}}} \left(\frac{P_{\text{gas}}}{\rho} - \psi_{\rho,\text{gas}} \epsilon_{\text{gas}} \right) \mathbf{v} \cdot \nabla \ln \rho - \frac{1}{\psi_{T,\text{gas}} \epsilon_{\text{gas}}} c \kappa_{\text{P}} \left(aT^4 - E_{\text{rad}}^{(0)} \right). \quad (\text{A4})$$

It is useful to rewrite the continuity equation (1a) into the following form

$$\nabla \cdot \mathbf{v} + \mathbf{v} \cdot \nabla \ln \rho = 0. \quad (\text{A5})$$

Taking the momentum equation (A1), utilizing the thermodynamics definitions (A3), plugging in equation (A4), and using the continuity equation (A5) gives

$$\mathbf{v} \cdot \nabla \left(\frac{1}{2} |\mathbf{v}|^2 \right) - \left(\chi_{\rho,\text{gas}} - \chi_{T,\text{gas}} \frac{\psi_{\rho,\text{gas}}}{\psi_{T,\text{gas}}} + \frac{\chi_{T,\text{gas}}}{\psi_{T,\text{gas}}} \frac{P_{\text{gas}}/\rho}{\epsilon_{\text{gas}}} \right) \frac{P_{\text{gas}}}{\rho} \nabla \cdot \mathbf{v} = \frac{\chi_{T,\text{gas}}}{\psi_{T,\text{gas}}} \frac{P_{\text{gas}}/\rho}{\epsilon_{\text{gas}}} c \kappa_{\text{P}} \left(aT^4 - E_{\text{rad}}^{(0)} \right) - \frac{\lambda}{\rho} \mathbf{v} \cdot \nabla E_{\text{rad}} - \mathbf{v} \cdot \nabla \phi_{\text{R}}. \quad (\text{A6})$$

The first velocity term in equation (A6) can be written as

$$\mathbf{v} \cdot \nabla \left(\frac{1}{2} |\mathbf{v}|^2 \right) = |\mathbf{v}|^2 \nabla \cdot \mathbf{v} - |\mathbf{v}|^3 \nabla \cdot \left(\frac{\mathbf{v}}{|\mathbf{v}|} \right). \quad (\text{A7})$$

Thus, using the definitions of q_{rad} and f_{rad} in equations (7,8) gives the 3D velocity equation for a general EOS that reads (cf. Lubow & Shu 1975, eq. 10)

$$\left[|\mathbf{v}|^2 - \left(\chi_{\rho,\text{gas}} - \chi_{T,\text{gas}} \frac{\psi_{\rho,\text{gas}}}{\psi_{T,\text{gas}}} + \frac{\chi_{T,\text{gas}}}{\psi_{T,\text{gas}}} \frac{P_{\text{gas}}/\rho}{\epsilon_{\text{gas}}} \right) \frac{P_{\text{gas}}}{\rho} \right] \nabla \cdot \mathbf{v} = |\mathbf{v}|^3 \nabla \cdot \left(\frac{\mathbf{v}}{|\mathbf{v}|} \right) - \frac{\chi_{T,\text{gas}}}{\psi_{T,\text{gas}}} \frac{P_{\text{gas}}/\rho}{\epsilon_{\text{gas}}} |\mathbf{v}| q_{\text{rad}} + \mathbf{v} \cdot f_{\text{rad}} - \mathbf{v} \cdot \nabla \phi_{\text{R}}. \quad (\text{A8})$$

If we use ideal gas EOS (equation 5), i.e. $\chi_{\rho,\text{gas}} = \chi_{T,\text{gas}} = \psi_{T,\text{gas}} = 1$ and $\psi_{\rho,\text{gas}} = 0$, and the definition of the gas adiabatic sound speed (equation 9) then we get the velocity equation (6).

APPENDIX B: DERIVATION OF 1D RADIATION HYDRODYNAMIC EQUATIONS AND 1D VELOCITY EQUATION

Under the assumptions described in Sec. 2.2, the divergence of a general vector field \mathbf{F}_{vec} and the gradient of a general scalar field f_{scal} are reduced to 1D as follows

$$\nabla \cdot \mathbf{F}_{\text{vec}} \rightarrow \frac{1}{Q} \frac{d}{dx} (Q F_{\text{vec}}), \quad \nabla f_{\text{scal}} \rightarrow \frac{df_{\text{scal}}}{dx}. \quad (\text{B1})$$

Therefore, the continuity equation (1a) trivially reduces to

$$\frac{1}{Q} \frac{d}{dx} (\rho v Q) = 0. \quad (\text{B2})$$

Reducing the momentum equation (1b) to 1D, using the previous equation (B2), and dividing the result by ρ yields

$$v \frac{dv}{dx} + \frac{1}{\rho} \frac{dP_{\text{gas}}}{dx} + \frac{\lambda}{\rho} \frac{dE_{\text{rad}}}{dx} = -\frac{d\phi_{\text{R}}}{dx}. \quad (\text{B3})$$

Reducing equation (1c) to 1D, using equation (B2), dividing the result by ρv , using the definition of the total gas specific energy ϵ^* in equation (2), and subtracting equation (B3) gives

$$\frac{d\epsilon_{\text{gas}}}{dx} - \frac{P_{\text{gas}}}{\rho} \frac{1}{\rho} \frac{d\rho}{dx} = -\frac{c}{v} \kappa_{\text{P}} \left(aT^4 - E_{\text{rad}}^{(0)} \right). \quad (\text{B4})$$

Summing up equations (1c) and (1d) and reducing the result to 1D yields a conservation law for the total luminosity being transferred through the nozzle L_N in the form $dL_N/dx = 0$. Therefore, the luminosity $L_N = \text{const.}$ is given by the equation

$$-\frac{c\lambda}{\rho\kappa_R} \frac{dE_{\text{rad}}}{dx} = \frac{L_N}{Q} - \left(\rho\epsilon^* + P_{\text{gas}} + \frac{3-f}{2} E_{\text{rad}} \right) v. \quad (\text{B5})$$

We can transform equations (B2–B5) into the set of 1D radiation hydrodynamic equations (11) by using simple manipulations and the definitions of q_{rad} and f_{rad} in equations (7,8).

Finally, reducing the velocity equation (A8) to 1D, canceling identical terms, and dividing it by v gives the 1D velocity equation for a general EOS in the form

$$\frac{1}{v} \frac{dv}{dx} = \frac{\left(\chi_{\rho,\text{gas}} - \chi_{T,\text{gas}} \frac{\psi_{\rho,\text{gas}}}{\psi_{T,\text{gas}}} + \frac{\chi_{T,\text{gas}}}{\psi_{T,\text{gas}}} \frac{P_{\text{gas}}/\rho}{\epsilon_{\text{gas}}} \right) \frac{P_{\text{gas}}}{\rho} \frac{1}{Q} \frac{dQ}{dx} - \frac{\chi_{T,\text{gas}}}{\psi_{T,\text{gas}}} \frac{P_{\text{gas}}/\rho}{\epsilon_{\text{gas}}} q_{\text{rad}} + f_{\text{rad}} - \frac{d\phi_R}{dx}}{v^2 - \left(\chi_{\rho,\text{gas}} - \chi_{T,\text{gas}} \frac{\psi_{\rho,\text{gas}}}{\psi_{T,\text{gas}}} + \frac{\chi_{T,\text{gas}}}{\psi_{T,\text{gas}}} \frac{P_{\text{gas}}/\rho}{\epsilon_{\text{gas}}} \right) \frac{P_{\text{gas}}}{\rho}}. \quad (\text{B6})$$

If we use ideal gas EOS (equation 5), i.e. $\chi_{\rho,\text{gas}} = \chi_{T,\text{gas}} = \psi_{T,\text{gas}} = 1$ and $\psi_{\rho,\text{gas}} = 0$, and the definition of the gas adiabatic sound speed (equation 9) then we get the velocity equation (14).

APPENDIX C: OUR PREVIOUS APPROACH AND OTHER MODELS

Here, we show the 1D hydrodynamic equations governing the gas flow in our original model (CP23) for convenience. The equations read

$$\frac{1}{v} \frac{dv}{dx} + \frac{1}{\rho Q_\rho} \frac{d}{dx}(\rho Q_\rho) = 0, \quad (\text{C1a})$$

$$v \frac{dv}{dx} + \frac{1}{\rho Q_\rho} \frac{d}{dx}(P Q_P) = - \frac{d\phi_R}{dx}, \quad (\text{C1b})$$

$$\frac{d}{dx} \left(\epsilon \frac{Q_P}{Q_\rho} \right) - \frac{P Q_P}{(\rho Q_\rho)^2} \frac{d}{dx}(\rho Q_\rho) = - \frac{d}{dx} \left(c_{T,\text{gas}}^2 \frac{Q_P}{Q_\rho} \right), \quad (\text{C1c})$$

where ϵ is the specific internal energy of the medium, gas plus radiation, and the characteristic cross-sections Q_ρ and Q_P corresponding to the density and pressure profiles respectively are defined by the following expressions

$$\rho(x)Q_\rho = \rho(x, 0, 0)Q_\rho(x) \equiv \int_{Q(x)} \rho(x, y, z)dQ, \quad (\text{C2a})$$

$$P(x)Q_P = P(x, 0, 0)Q_P(x) \equiv \int_{Q(x)} P(x, y, z)dQ. \quad (\text{C2b})$$

It holds

$$Q_\rho = \frac{2\pi}{\sqrt{BC}} c_{T,\text{gas}}^2, \quad \frac{Q_P}{Q_\rho} = \frac{\gamma}{2\gamma-1}. \quad (\text{C3})$$

The optically thin MT rate of Jackson et al. (2017) is given by

$$-\dot{M}_d \equiv \dot{M}_J = \dot{M}_{J,0} \exp \left(-\frac{\phi_1 - \phi_{\text{ph}}}{c_{T,\text{gas}}^2} \right), \quad \dot{M}_{J,0} = \frac{2\pi}{\sqrt{e}} \frac{1}{\sqrt{BC}} c_{T,\text{gas}}^3 \rho_{\text{ph}}, \quad (\text{C4})$$

where the potential difference between the L1 point ϕ_1 and the photosphere ϕ_{ph} is evaluated based on the following approximation

$$\phi_V(r_V) = -G \frac{M_a}{a} \left[1 + \frac{1}{2(1+q)} \right] - G \frac{M_d}{r_V} \left[1 + \frac{1}{3} \left(1 + \frac{1}{q} \right) \left(\frac{r_v}{a} \right)^3 + \frac{4}{45} \left(1 + \frac{5}{q} + \frac{13}{q^2} \right) \left(\frac{r_v}{a} \right)^6 \right], \quad (\text{C5})$$

where the volume-equivalent radius r_V is defined using a sphere with a volume V enclosed by the equipotential surface on the donor's side of the L1 plane, $V(\phi_V) = 4\pi r_V^3/3$. The optically thick MT rate of Kolb & Ritter (1990) is given by

$$-\dot{M}_d \equiv \dot{M}_{KR} = \dot{M}_{J,0} + \frac{2\pi}{\sqrt{BC}} \int_{P_{\text{ph}}}^{\bar{P}(R_L)} F_3(\gamma) c_{T,\text{gas}} d\bar{P}, \quad \text{where } F_3(\gamma) = \gamma^{\frac{1}{2}} \left(\frac{2}{\gamma+1} \right)^{\frac{\gamma+1}{2(\gamma-1)}}, \quad (\text{C6})$$

and to calculate \dot{M}_J and \dot{M}_{KR} an ideal gas EOS is used to evaluate $c_{T,\text{gas}}$, see equation (5).

APPENDIX D: 1 M_⊙ DONOR ON THE RED GIANT BRANCH

We use MESA version r21.12.1 and its 1M_pre_ms_to_wd test suite case to compute hydrostatic profiles of a donor star with initial mass 1 M_⊙ and metallicity $Z = 0.02$. We evolve the stellar model to an age of 12.3 Gyr, when we obtain a red giant with the effective temperature $T_{\text{eff}} = 3.4 \times 10^3$ K, radius $R_d = 89 R_\odot$, luminosity $L_d = 1.0 \times 10^3 L_\odot$, and Eddington ratio Γ_{Edd} at the surface of 1.8×10^{-4} .

In Fig. D1, we compare $\dot{M}_{\text{an,thin}}(\Delta R_d)$ and $\dot{M}_{\text{an,thick}}(\Delta R_d)$ with the models of Jackson et al. (2017) (\dot{M}_J) and Kolb & Ritter (1990) (\dot{M}_{KR}). The photospheric pressure scale height in this case is $H_{P,\text{ph}} = 0.011 R_d = 0.96 R_\odot$. We see, as expected, that for a gas pressure dominated envelope, $P_{\text{gas}} \gg P_{\text{rad}}$, the differences between the two models are small (to within 20 %).

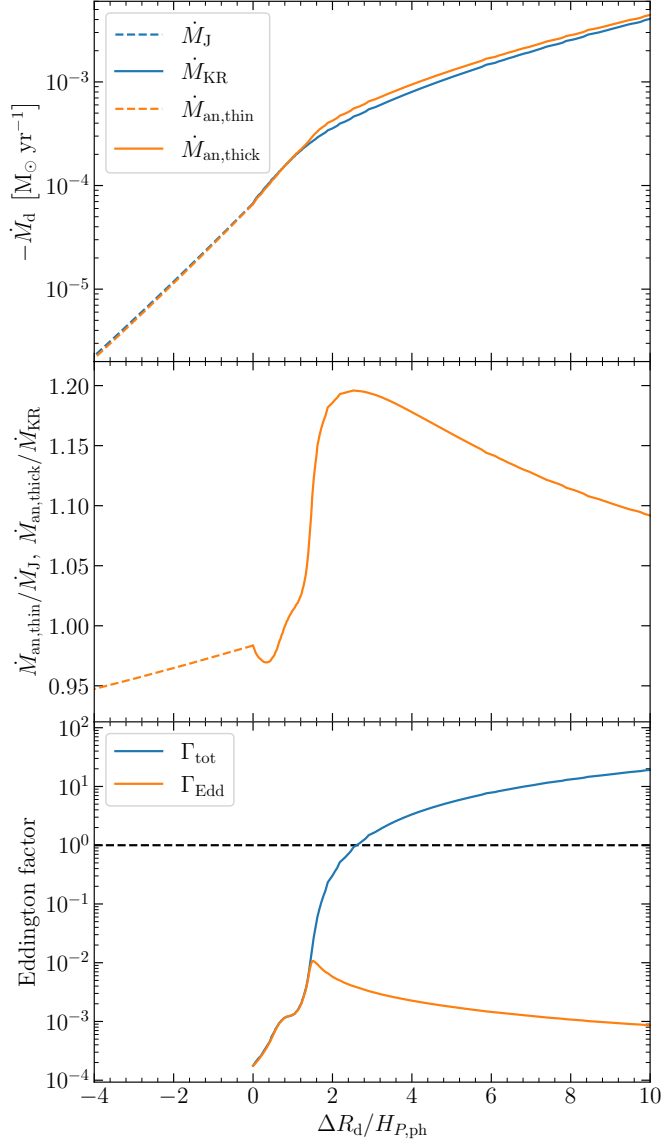


Figure D1. Comparison of our analytical MT prescription $\dot{M}_{\text{an},\text{thin}}$ and $\dot{M}_{\text{an},\text{thick}}$ with the optically thin prescription introduced by Jackson et al. (2017), \dot{M}_J , and the optically thick prescription introduced by Kolb & Ritter (1990), \dot{M}_{KR} . We also show the total Eddington factor $\Gamma_{\text{tot}} = L/L_{\text{Edd}}$ and the Eddington factor Γ_{Edd} (equation 28) for comparison. The case shown is for an isolated $1M_\odot$ solar-like star on the red giant branch.

APPENDIX E: DERIVATION OF THE MODIFIED PHOTON-TIRING LIMIT

Here, we present the derivation of the photon-tiring limit modified for the MT through the L1 point, $\dot{M}_{\text{tir,L1}}$ (equation 47). We approximate the total luminosity transferred through the nozzle around L1 by

$$L_N = L_d \frac{Q}{4\pi R_d^2}, \quad (E1)$$

where Q is the nozzle cross-section given by equation (30) and $4\pi R_d^2$ is the surface area of the donor. The quantities in the equation (30) needed to evaluate Q can be approximated as follows (Jackson et al. 2017, but see also CP23)

$$B = (\mathcal{A} - 1)\omega^2, \quad C = \mathcal{A}\omega^2, \quad \mathcal{A} = 4 + \frac{4.16}{-0.96 + q^{1/3} + q^{-1/3}}, \quad \omega^2 = \frac{GM}{a^3}, \quad (E2)$$

where $M = M_a + M_d$ is the total binary mass comprising of the accretor's and the donor's mass, $q = M_d/M_a$ is the binary mass ratio, and a is the binary separation that can be approximated by (Eggleton 1983)

$$a = \frac{R_L}{f(q)}, \quad \text{where } f(q) = \frac{0.49q^{2/3}}{0.6q^{2/3} + \ln(1 + q^{1/3})}. \quad (E3)$$

Using these approximations we write

$$\sqrt{BC} = \sqrt{\mathcal{A}(\mathcal{A} - 1)} \left(1 + \frac{1}{q}\right) f^3(q) \frac{GM_d}{R_L^3} = f_1(q) \frac{GM_d}{R_L^3} \approx \frac{GM_d}{R_d^3}, \quad (\text{E4})$$

where in the last approximate equation we neglect $f_1(q)$ since it holds $f_1(q) \in \langle 0.5, 1.7 \rangle$, for $q \in \langle 10^{-2}, 10^2 \rangle$, and use $R_L \approx R_d$. Putting together the approximation for L_N in equation (E1), the definition of Q in equation (30), but omitting the $1/(1 - \Gamma_{\text{Edd}})$ factor because the luminosity being transferred through the nozzle L_N cannot diverge for $\Gamma_{\text{Edd}} \rightarrow 1$, and equation (E4) we get to order of magnitude

$$L_N \sim L_d \frac{c_{T,\text{gas}}^2}{v_{\text{esc}}^2}. \quad (\text{E5})$$

To approximate the potential difference between R_L and R_{SE} inside the donor, we can write

$$\bar{\phi}(R_L) - \bar{\phi}(R_{\text{SE}}) = -\frac{GM_d}{R_L} + \frac{GM_d}{R_{\text{SE}}} \approx \frac{1}{2} v_{\text{esc}}^2 \delta R_L, \quad (\text{E6})$$

where we again use $R_L \approx R_d$ and $\delta R_L \equiv (R_L - R_{\text{SE}})/R_{\text{SE}}$.

This paper has been typeset from a $\text{TeX}/\text{\LaTeX}$ file prepared by the author.